Development of Novel Image Analysis and Modeling Tools to Examine Mechanisms of Muscle Damage in Duchenne Muscular Dystrophy

---

A Thesis

Presented to

the Faculty of the School of Engineering and Applied Science

University of Virginia

In Partial Fulfillment of the requirements

for the Degree

Master of Science

by

Emily Y. Miller

August 2019

APPROVAL SHEET

This Thesis
is submitted in partial fulfillment of the requirements
for the degree of
Master of Science

Author Signature: 

This Thesis has been read and approved by the examining committee:

Advisor: Silvia S. Blemker

Committee Member: Shayn Peirce-Cottler

Committee Member: Jason Kerrigan

Committee Member: _____

Committee Member: _____

Committee Member: _____

Accepted for the School of Engineering and Applied Science:

Craig H. Benson, School of Engineering and Applied Science

May 2019

UNIVERSITY OF VIRGINIA

Development of Novel Image Analysis and Modeling Tools to Examine Mechanisms of Muscle Damage in Duchenne Muscular Dystrophy

A THESIS

SUBMITTED TO THE GRADUATE SCHOOL
IN PARTIAL FULLFILLMENT OF THE REQUIREMENTS

for the degree

MASTER OF SCIENCE

Field of Biomedical Engineering

By

Emily Y. Miller

CHARLOTTESVILLE, VIRGINIA

August 2019

Abstract

DMD is a devastating X-linked recessive musculoskeletal disorder that effects 1 in 3500 boys [1]. DMD is caused by the lack of a functional dystrophin protein, a structural protein that mechanically links muscle fibers to the extracellular material. Without dystrophin, muscle fibers are more susceptible to contraction induced damage [2], [3].Therefore, everyday movements such as walking, talking, and breathing result in cycles of muscle degeneration and regeneration, ultimately leaving affected individuals wheelchair users by their early teens, and at high risk for respiratory or cardiac failure in their second or third decade of life [4]. Muscle fibers, the central cellular unit of muscle, change their morphologies and geometric arrangements in ways visibly discernable using immunofluorescence microscopy in response to external stimuli or changing functional demands. Therefore, analysis of these geometrical differences can provide insight into the structure-function relationships present in skeletal muscle.

Computational models provide a powerful paradigm to understand muscle degeneration and explore possible treatment approaches for Duchenne muscular dystrophy (DMD). This thesis contains two sections. First, I designed, developed, and validated a new skeletal muscle image processing algorithm to detect muscle fiber boundaries in skeletal muscle histological cross-sections. The algorithm is capable of whole muscle cross-section microstructure analysis, and was validated against a standard muscle histological manual analysis and two open-sourced currently available skeletal muscle analysis software programs. Then, I utilized this algorithm to build micromechanical finite element models of real skeletal muscle microstructures of both dystrophic and healthy full muscle-cross-sections to explore how muscle fiber morphologies and geometric arrangements affect the

susceptibility of dystrophic and healthy muscles to contraction induced-damage. The models predicted that decreased muscle fiber cross-sectional areas, increased muscle fiber circularity and increased variability of muscle fiber cross-sectional areas, increase the susceptibility to contraction-induced damage of a given muscle.

Ultimately, I have developed in this thesis a skeletal muscle image analysis tool that outperforms the current available programs and has already been adapted by two other research groups at UVA and developed micromechanical models that can be used to investigate the role of muscle microstructure in DMD pathogenesis. This work provides a framework to determine micro-scale damage from microstructure images and could be used to model the effect of pharmacological treatments on DMD damage susceptibility and therefore lays the groundwork for future work in *in silico* testing of therapeutics for DMD.

Acknowledgments

I feel extremely lucky to have started on my path to engineering at the University of Virginia, joining the Biomedical Engineering department and the Multiscale Muscle Mechanophysiology lab. The past two years at UVA have been transformative in my academic and personal growth and none of this would have been possible without the many people who have supported me on this journey.

First and foremost, I would like to thank my advisor, Dr. Silvia Blemker, for your relentless positivity and mentorship. You have been a wonderful role model. I appreciate the way you have allowed me to explore problems that interest me, and allowed me to chart a course through my research. You have taught me so much about scientific research and biomechanics. I appreciate your scientific enthusiasm. I'd also like to thank you for allowing me to pursue a somewhat unconventional first semester at UVA, and join the UVA field hockey team for a semester. Overall, thank you for your mentorship, for giving me the opportunity to join the M3 lab, and for taking a chance on a biology major with no engineering experience.

I would also like to thank my Master's committee: Dr. Shayn Peirce-Cottler and Dr. Jason Kerrigan. Shayn, I am truly grateful for your support throughout my two years at UVA, from my first physiology class with you, to your guidance throughout my research. Thank you for reaching out after my 4S presentation and bringing me in to the VT project. This project would have been a very different one without your support. Jason, while taking your continuum mechanics course (my first mechanical engineering course ever), I decided to look into PhD programs in mechanical engineering. You taught me so much about mechanics in a way that was incredible accessible to someone without an undergraduate engineering background. I learned so much from you in that class, and it gave me the confidence to pursue

further study in mechanical engineering. I also greatly appreciate the meetings I've had with you in the past few months, they helped me greatly in thinking about the work in this thesis from a more mechanics-based perspective. Outside of UVA, this work would not have been completed without the assistance of our collaborators at Virginia Tech, especially Dr. Rob Grange, Kate Bukovec, and Daniel Fathalikhani. In particular I'd like to thank Rob for his insights in muscle physiology. I also would like to thank Kate for the use of her histological images, and Dan for assisting in the manual validation of the algorithm presented in this work.

I am truly grateful for the support and insight from the current and former members of the Multiscale Muscle Mechanophysiology Lab. I have learned so much from all of you and I will miss the support (and humor) in our lab. It's been a great place to be during these past two years. In particular, I would like to thank Kelley Virgilio and Brian Jones for their mentorship and support in my time at UVA. In the beginning I know how many questions I asked both of you, and I appreciate your willingness to teach me about biomechanics and modeling. To my parents, thank you for your constant support through the past two years and throughout my life. Thank you for never doubting my ability to succeed, even when I was frustrated and confused. I appreciate your continuous encouragement. Your guidance and support have been pivotal to the completion of this thesis.

Contents

List of Figures

List of Tables

List of Equations

Chapter 1

Introduction

Skeletal muscle function is fundamentally important for human health and ability, accounting for approximately 40 percent of total body mass in the human adult [5], [6]. Daily life activities such as speech, breathing, and movement are facilitated by healthy muscle function. Loss of skeletal muscle function can lead to disability, impaired quality of life, and death. Skeletal muscle is organized in a complex hierarchical structure, wherein the predominant cell is the muscle fiber. Muscle fibers are highly adaptable to external stimuli and changing functional demands, changing their shapes, sizes, and geometrical arrangements in response. Injury, exercise, disease, spaceflight, and aging can alter skeletal muscle microstructure composition in ways that are visually discernible using immunofluorescence microscopy (Figure 1.1) [7], [8]. As muscle fibers adapt to external stimuli, numerous research groups seek to measure fiber-morphology as part of their muscle analyses to better understand muscle microstructure adaptation.

Muscle microstructures are altered by many diseases, including Duchenne muscular dystrophy. Duchenne muscular dystrophy (DMD) is a genetic X-linked disorder that causes progressive muscle degeneration and weakness, affecting 1 in 3500 boys [9]. It is caused by the incomplete translation of the dystrophin protein, resulting in absent or damaged dystrophin linkage protein, which links the muscle fiber membrane to the surrounding ECM [10]. Without the dystrophin protein, muscle is more susceptible to contraction-

induced damage, and as a result everyday movements such as walking and breathing result in cycles of muscle degeneration and regeneration, ultimately resulting in chronic inflammation, fibrosis, and muscle wasting [11].

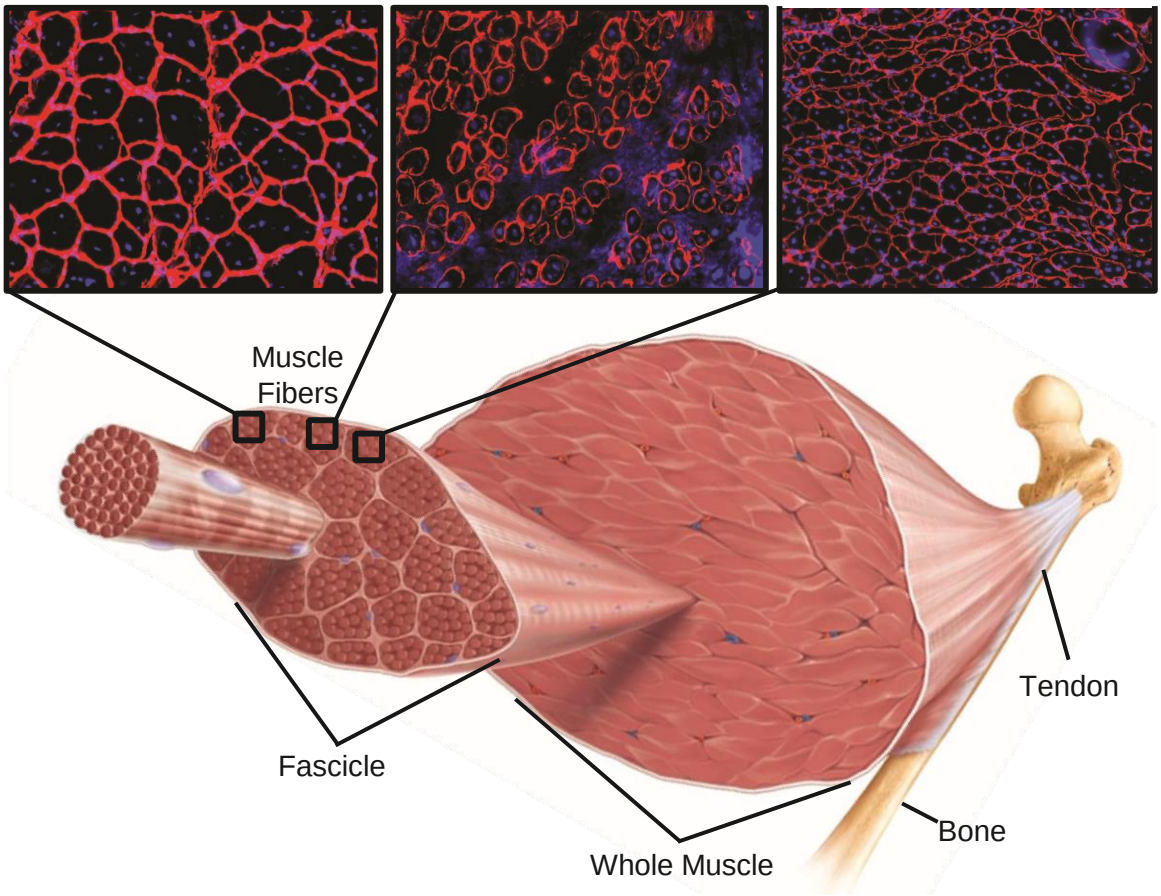

Figure 1.1: Skeletal Muscle Structure and Varying Muscle Fiber Morphologies in the Transverse View. Skeletal muscle is organized in a hierarchical structure consisting of highly organized repeating structures, with the muscle fiber the central cellular unit of muscle tissue. The top row displays images of murine muscle fibers morphologies. Images are confocal images of Laminin2 and DAPI stained muscle cross sections. Muscle fibers are outlined in red, with nuclei shown in blue. Scale: 420 μm by 564 μm. Figure adapted from Encyclopedia Britannica 2015.

Computational models provide a powerful paradigm to understand muscle degeneration and explore possible treatment approaches for DMD. The hierarchical structure of skeletal muscle lends itself to computational modeling. Computational models

of muscle have been built at many scales, from simplified multiple muscle models, to finite element models of whole muscle, muscle fascicles, or fibers, to models of the interactions of individual proteins [12]–[16]. While the microstructure of skeletal muscle has been extensively studied at different levels, many questions remain regarding the relationship between muscle microstructure properties and muscle function. Disease, ageing, exercise, and other environmental factors can alter the shapes and geometrical arrangement of muscle fibers and their connective tissues in ways that vary significantly across muscles. How these variations affect the macroscopic properties of muscle and muscle's susceptibility to damage is not well understood.

Recently, finite element (FE) models of skeletal muscle microstructure were developed to explain the susceptibility of DMD muscles to contraction-incurred damage [4], [17]–[19]. However, these works explored muscle microstructure at a scale of approximately 30 or fewer muscle fibers. Full muscle cross sections, as seen in Figure 1.2 consist of many hundreds of muscle fibers. Therefore, building upon this previous work, the purpose of this thesis is to create finite element models of based on real images of skeletal muscle microstructures in both dystrophic and healthy full muscle-cross-sections consisting of hundreds of muscle fibers to explore how real microstructure variations affect the susceptibility of dystrophic and healthy muscles to contraction induced-damage. To facilitate the creation of the image-based full-muscle cross-section FE models, this thesis also presents a novel semi-automatic segmentation algorithm to detect muscle fiber boundaries in skeletal muscle histological cross-sections. The utilization of the skeletal muscle analysis algorithm allows for the micromechanical FE modeling of whole muscle

cross-sections consisting of several hundred muscle fibers, a far larger scale than previously attempted.

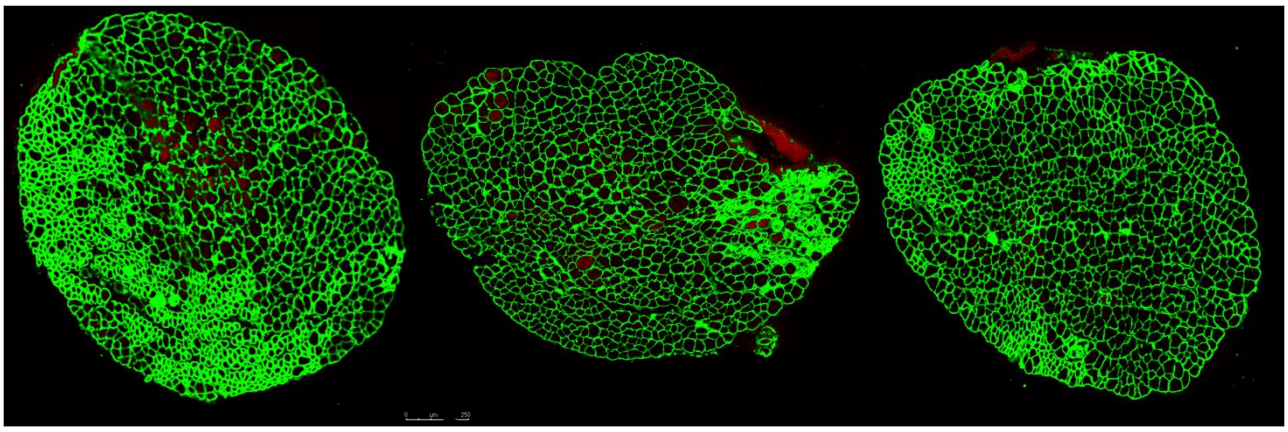

Figure 1.2: Images of mouse skeletal muscle cross-sections in the transverse view. Mouse whole muscle cross-sections consist of many hundreds of muscle fibers. Due to the small size of mouse muscles, fascicle structures are not present. All three muscles are murine extensor digitorum longus (edl) muscles. Fiber boundaries (green) were stained and visualized with Laminin-2α.

This thesis contains four subsequent chapters. Chapter 2 presents background sections describing Duchenne muscular dystrophy, the existing approaches to modeling skeletal muscle, the constitutive model used in chapter 4 to represent muscle fibers and extracellular material, the micromechanical modeling approach employed in Chapter 4, and existing approaches to image processing of skeletal muscle histology. Chapter 3 presents the design of the semi-automatic skeletal muscle analysis algorithm, the validation of the algorithm, and analysis of algorithm segmentation performance and operation time. In Chapter 4, finite element models of skeletal muscle microstructures were developed to study the effect of muscle fiber geometries on the susceptibility of dystrophic and healthy muscles to contraction-incurred damage. Chapter 5, the conclusion, discusses the contributions of this thesis to the understanding of muscle structure and function and describes further applications of the work presented here.

Chapter 2

Background

2.1 Skeletal muscle structure

Skeletal muscle has a complex hierarchical structure where at each scale contractile, force-producing muscle tissue is surrounded by a network of structurally supportive extracellular material (Figure 2.1). The smallest force producing unit of muscle is the sarcomere. Muscle sarcomeres are the contractile units of muscle and are composed of thick and thin filament proteins called myosin and actin respectively, as well as titin, which acts as a spring as well as to provide passive stiffness to the sarcomere [20], [21]. As shown in Figure 2.2, when actin and myosin slide with respect to one another, using adenosine tri-phosphate as a source of energy, the sarcomere contracts [22]. This overlap of thick and thin filaments gives rise to the force-length and force-velocity relationships that define the force-generating capacity of muscle [23]. Sarcomeres stack to form long multi-nucleated muscle cells, incased by the cell membrane (also called the sarcolemma), that are also known as muscle fibers [21]. A muscle fiber contraction is caused by the simultaneous contraction of all of its sarcomeres. Muscle fibers are bundled together in multi-fiber groups called fascicles and fascicles are bundled together to form the whole muscle. Muscle fibers and fascicles are embedded in an intramuscular connective tissue matrix called the extracellular matrix (ECM) [24]. ECM consists of two connective tissues, known as the

endomysium and perimysium [25]. ECM is thought to play a critical role in enabling force transmission from fibers to tendon and in protecting muscle cells from excessive damage during muscle contractions. The shapes and geometries of muscle fibers, fascicles, and connective tissues vary significantly across muscles [7]. These geometries are altered by disease, ageing, exercise, as well as environmental exposures [7], [8], [26]. Therefore, analysis of these geometrical differences can provide insight into the structure-function relationships present in skeletal muscle.

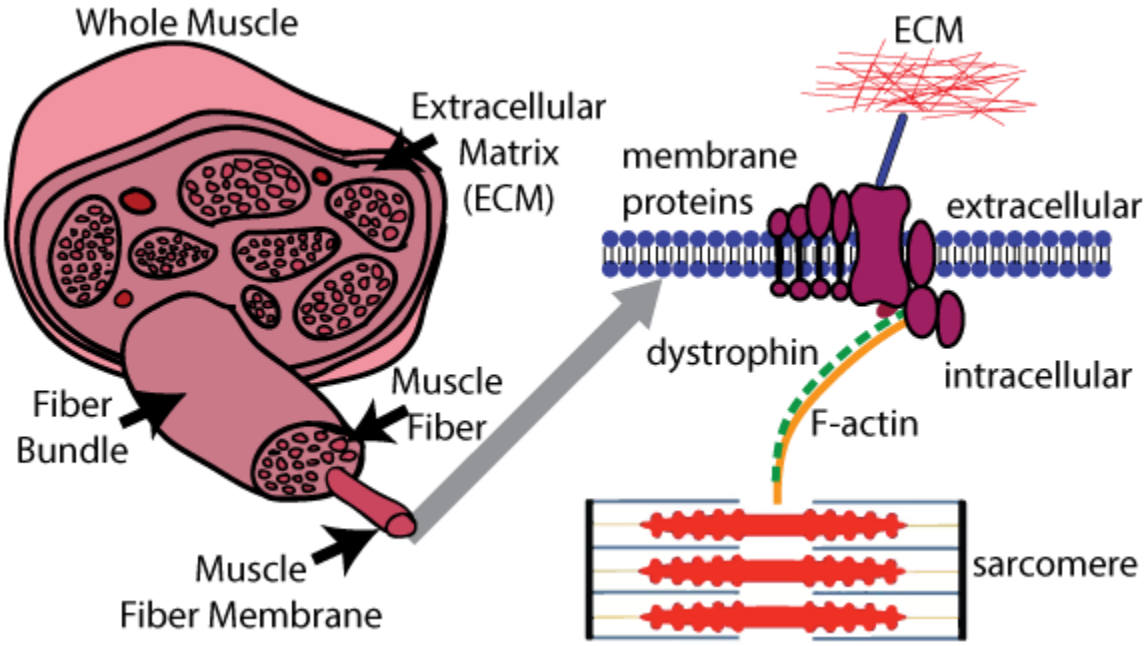

Figure 2.1: The Hierarchical Structure of Skeletal Muscle. Skeletal muscle has a complex hierarchical structure where at each scale contractile, force-producing muscle tissue is surrounded by a network of structurally supportive extracellular material. Muscle fiber membranes (also called sarcolemna) contain transmembrane protein complexes containing the dystrophin protein that links sarcomeres to the cell membrane and extracellular material (ECM).

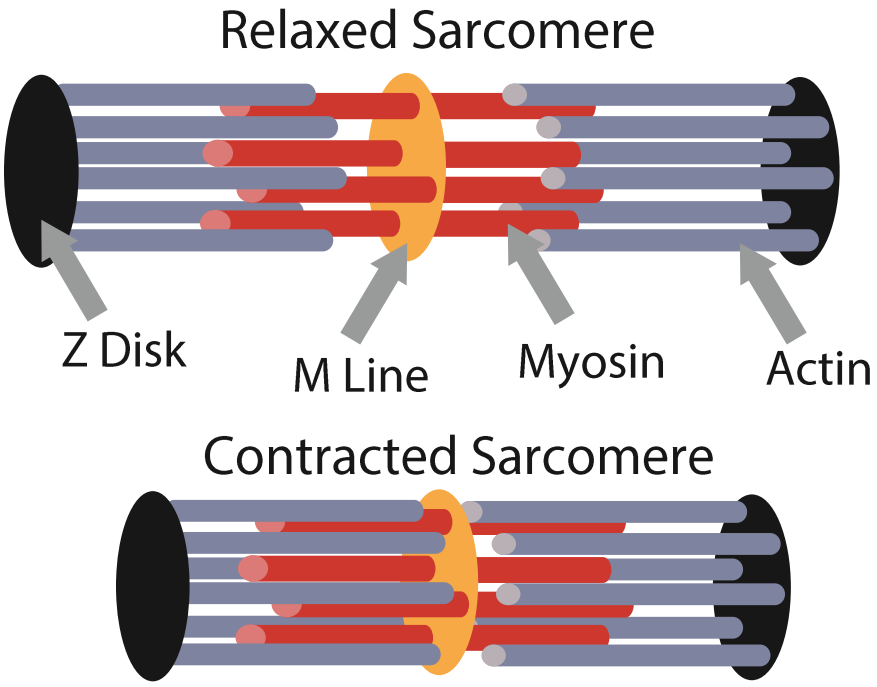

Figure 2.2: The contractile sarcomere is the smallest force producing unit in muscle. Sarcomeres are the basic unit of striated muscle tissue. The basic repeating unit occurs between two z-disks (also called z-lines).

2.2 Duchenne muscular dystrophy

Skeletal muscle accounts for approximately 40 percent of a human body mass and is a facilitator of daily life activities [6]. Skeletal muscle enables movement of the human body, from walking to talking to breathing. Therefore, diseases that disrupt healthy muscle function can have a devastating effect on quality of life. Duchenne muscular dystrophy (DMD) is a devastating X-linked recessive musculoskeletal disorder that effects 1 in 3500 boys [1]. Symptoms of DMD manifest around ages 3-5 when boys exhibit changes in walking patterns. Muscle function progressively degenerates until most affected individuals are wheelchair users by their early teens, and die due to respiratory or cardiac failure in their second or third decade of life [1], [4]. The current standard of care for DMD is corticosteroid

injections, which is only palliative and prescribed to delay the use of a wheelchair [9]. While the cause of DMD, a hereditary biochemical defect of muscle tissue, has been known since the 1980s, there is no cure for DMD despite extensive experimental research [1].

DMD is caused by the lack of a functional dystrophin protein, a structural protein that mechanically links muscle fibers to the extracellular material [27]. The dystrophin gene is the largest gene in the human genome, spanning roughly 2200 kb and 0.1 percent of the human genome [28]. The most common causes of DMD are exon deletions and point mutations within the dystrophin gene [10]. These genetic mutations cause the dystrophin protein to have premature stop-codons, and the protein is then truncated to be shorter than its functional length. These truncated proteins are unstable and subject to degradation, leaving little to no dystrophin protein left within cells [10]. Individuals with DMD either lack the dystrophin protein completely, or the protein is present in small quantities. Lacking the mechanical link between muscle fibers and ECM, dystrophic muscle is more susceptible to contraction induced damage [2], [3]. Therefore, everyday movements such as walking, talking, and breathing result in cycles of muscle degeneration and regeneration. DMD muscle biopsies have shown necrotic or degenerating muscle fibers even before muscle weakness is clinically observed [29]. Following muscle fiber necrosis, in the early stages of DMD, active regeneration of muscle fibers will occur to repair damaged muscle fibers. These cycles of degeneration and regeneration occur until the muscle tissue loses its regenerative capability [29]. When the regenerative capability of the muscle tissue is lost, muscle fibers are replaced by adipose and fibrotic tissues. The combination of progressive muscle loss with fibrosis and fat infiltration leads to muscle wasting and weakness [29].

2.3 Modeling of skeletal muscle

Computational models provide a powerful paradigm to understand muscle degeneration and explore possible treatment approaches for Duchenne muscular dystrophy (DMD). In the past two decades, computational models of skeletal muscle have advanced significantly and these simulations provide a powerful tool for understanding human movement and its disorders. Biomechanical simulations have been used to test and predict the effect of disease, injury, exercise intervention, and surgical treatments [13], [14], [30]–[33]. In muscle, the purpose of computational modelling is to simulate the active force generation and passive properties that are inherent characteristics [22], [34]. The first computational models of skeletal muscle were Hill-type models that describe, in a phenomenological manner, the active force-length velocity behavior of whole muscles [23], [35]. Hill type models have been most often used in computer models involving several muscles, representing each muscle as line-segment. In these lumped-parameter models (i.e. OpenSim), the active force-length velocity behavior of muscle is represented by a contractile (active) element governed by the force-length and force-velocity relationships described by Hill, as well as series and parallel passive stiffness components [16], [35]–[37]. While these models are useful for multi-muscle simulations used in the study of human movement because they reduce the computational complexity required for simulation of movement, they neglect to account for non-uniform sarcomere shortening, and are poor at representing the behavior of muscles with complex geometries [20]. To more accurately model the distribution of strains within muscle tissue, three-dimensional continuum models of muscle were developed to address these limitations.

Continuum models of muscle represent the nonlinear anisotropic mechanical behavior of muscle in a continuum mechanics-based framework [38]. Advances in MRI have allowed for the realistic three-dimensional representation of muscles with complex geometries to be possible [31], [39]. Models using these advanced geometrical representations of muscle and treating muscle as a continuum have been used to study non-uniform stress distributions, myofascial force transmission, and intramuscular pressure. However, these constitutive models of muscle lump the properties of muscle fibers and the intramuscular extracellular material into one constitutive relationship that assumes a transversely isotropic material microstructure [40]. The constitutive relationship is not derived from the muscle microstructure properties, it is phenomenological. While these models do an excellent job at accounting for macroscopic muscle properties, as muscle cells and connective tissues are not explicitly defined in the model, they are limited in their capacity to relate disease-related muscle changes to biomechanical changes at the molecular and cellular level. To remedy these limitations, recently micromechanical models of muscle have been developed to better study the relationship between muscles complex hierarchical microstructure and macroscopic function [4], [17]–[19]

2.3.1 Micromechanics

Micromechanics is the study of composite materials made up of heterogeneous constituents, at the level of the individual constituents that make up the materials [41]. Skeletal muscle can be thought of as a fibrous composite composed of intramuscular connective tissue playing the role of the matrix and muscle fibers as the fibrous reinforcements [25], [42], [43]. The purpose of micromechanical analysis is to predict the macroscopic properties of the composite material, given the material properties and

geometry of the constituent elements of the microstructure. In this work, we have applied the methods used in micromechanical analysis to the study of skeletal muscle. Micromechanical models of skeletal muscle allow us to explicitly represent the microstructure of muscle fibers and fascicles and are necessary to explore how the complex structure of muscle fibers affects muscle function.

Various analytical and computational methods have been used to solve micromechanics problems, included finite elements. The advantages of the finite element approach are that the actual geometries can be modeled and stress and strain distributions can be predicted. The micromechanical muscle modeling framework utilizes the concepts of repeating unit cells (RUCs) and periodic boundary conditions to examine damage susceptibility from finite element (FE) models of muscle microstructures [17]. This method assumes that the composite material, skeletal muscle, is spatially periodic and can be thought of as many repetitions of a periodic unit cell that remains periodic while deforming. Due to the hierarchical structure of muscle, consisting of long multinucleated muscle fibers, each consisting of multiple sarcomeres, this assumption holds.

Through micromechanical modeling we can investigate the mechanisms through which DMD disease-related changes to muscle fiber geometries alter whole level muscle properties. At the fascicle level, Sharafi et al. used micromechanical models that separate muscle fibers and ECM to investigate how changes in muscle microstructure affect tissue level material properties [17]. Building upon that work, Virgilio et al used micromechanical models to probe how DMD related disease changes would alter tissue level properties and damage susceptibility[4] . However, the micromechanical models built by Virgilio et al. were not based upon real muscle cross-sections, they were based upon pseudo-muscle cross

sections generated from an agent-based model. Furthermore, the micromechanical models built by both Sharafi et al. and Virgilio et al. both consisted of less than thirty muscle fibers per model. Therefore, we have used the works of both Sharafi et al. and Virgilio et al. to build micromechanical models based upon based upon real whole muscle cross-sections, each consisting of several hundred muscle fibers to probe how DMD-related changes in real muscle microstructure affect the damage susceptibility of muscle.

2.3.2 Constitutive model for muscle fibers and intramuscular connective tissue

The muscle fibers and intramuscular connective tissues in the finite element models presented here have been modeled as transversely isotropic, hyperelastic, nearly incompressible materials [44]. These assumptions are common in the modeling of both muscle tissue and connective tissues [40]. In hyperelastic materials, stress and strain are related by:

$$\boldsymbol{S} = 2\frac{\partial \boldsymbol{W}}{\partial \boldsymbol{C}} \tag{1}$$

where stresses are derived from the strain energy density function **W**, the second Piola-Kirchoff stress tensor **S**, and the right Cauchy-Green strain tensor **C**. The deformation gradient **F**, and right Cauchy-Green deformation tensor **C**, are respectively defined as,

$$\boldsymbol{F} = \frac{\partial x}{\partial X} \tag{2}$$

$$\boldsymbol{C} = \boldsymbol{F}^T \boldsymbol{F} \tag{3}$$

where x represents the deformed vector and X represents the reference vector. The constitutive model uses an uncoupled form of the strain energy density function to simulate the near incompressible behavior of both the muscle tissue and intramuscular connective

tissue. The strain energy density function separates the dilatational (volumetric) and deviatoric (distortional) responses of the muscle tissue, resulting in the following strain energy density function:

$$\boldsymbol{W}(\lambda, \psi, \beta, J) = \boldsymbol{W}_{\lambda}(\lambda) + \boldsymbol{W}_{\psi}(\psi) + \boldsymbol{W}_{\beta}(\beta) + \boldsymbol{W}_{J}(J) \quad (4)$$

where λ is the along-fiber stretch, ψ is the along-fiber shear, β is the cross-fiber shear and J is the relative change in volume of the tissue. The fiber direction is defined along the axis of transverse isotropy. In this model it is assumed to run along the path of the muscle for both ECM and muscle fibers. Physically based strain invariants (Figure 2.3) were used to relate material parameters to experimentally quantifiable measurements [45].

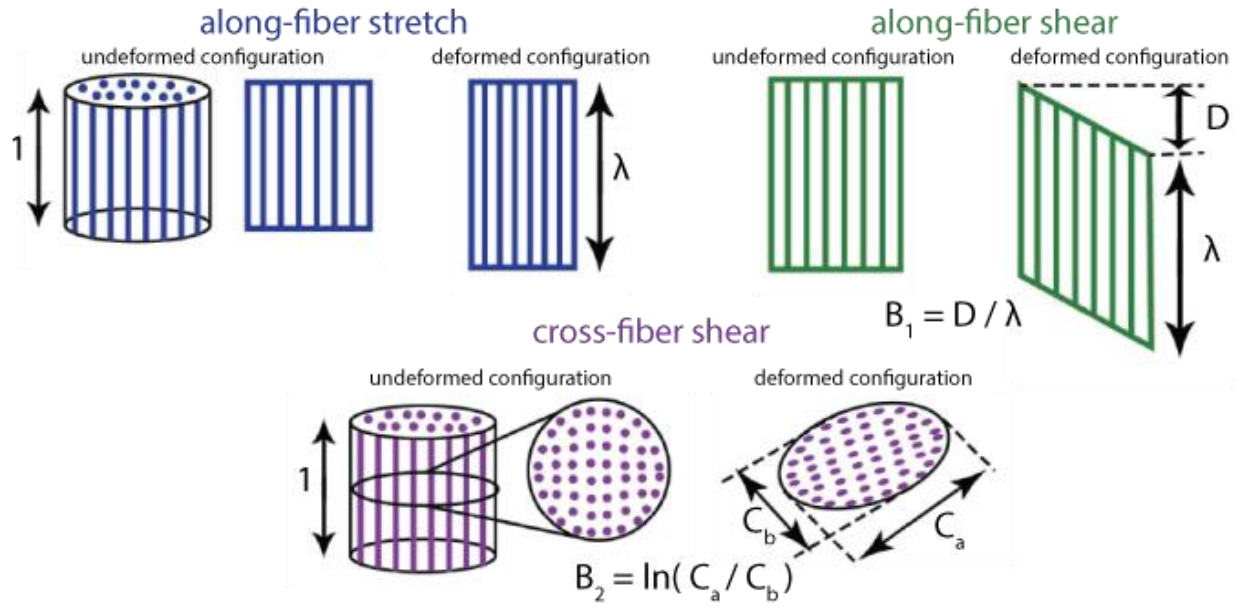

Figure 2.3: Physically-based strain invariants. The above strain invariants were used as part of the constitutive model for muscle. They characterize the along fiber stretch, along-fiber simple shear strain, and cross fiber pure shear strain [40].

$\mathbf{W}_{\lambda}(\lambda)$ is a piece-wise function representing the passive material properties of the tissue, dependent on the fiber length. $\mathbf{W}_{\psi}(\psi)$, $\mathbf{W}_{\beta}(\beta)$, and $\mathbf{W}_{J}(J)$ were defined as follows:

$$W_{\psi}(\psi) = G_{\psi}\psi^2 \tag{5}$$

$$W_{\beta}(\beta) = G_{\beta}\beta^2 \tag{6}$$

$$W_J = \frac{K}{2}\ln J^2 \tag{7}$$

where G_{ψ} is the along-fiber shear modulus, G_{β} is the cross-fiber shear modulus and K is the bulk modulus and J is the relative change in volume [40]. FE simulations are quasi-static and do not account for viscoelasticity [46].

2.4 Analysis of skeletal muscle cross section images

The ability to create finite-element models from images of muscle cross-section fiber geometries for the finite element models requires a semi-automatic image segmentation algorithm that performs a high content analysis of skeletal muscle immunohistochemical images. Analysis of skeletal muscle cross sections is an important experimental technique in muscle biology. Muscle fibers adapt to external stimuli and changing functional demands and many different conditions modulate skeletal muscle fibers in ways that are visually discernible using immunofluorescence microscopy. Numerous research groups, besides our own, seek to measure fiber-morphology as part of their muscle analyses. In particular, muscle fiber cross-sectional areas (CSA) are commonly used as a metric for muscle regeneration in experiments studying disease or injury pathologies [7].

However, most image quantification techniques still require extensive and time consuming human supervision, which can increase variability of results and introduce the possibility for user bias in results. Traditionally, the quantification of muscle fiber CSA is done manually in software such as ImageJ by outlining each and every fiber [7]. This introduces variability due to limits on manual dexterity and the possibility of user bias. Furthermore, in studies with full-muscle cross-sectional images consisting of hundreds to

thousands of muscle fibers, a manual segmentation is a painstaking, inefficient, and tedious endeavor. While manual segmentation is considered to be the gold-standard in the field, in large experimental studies it is not an easily viable solution.

Two groups have created open-source computer software that can expedite the process of skeletal muscle cross-section analysis by measuring muscle fiber numbers and areas. Both SMASH software, written by Smith and Barton, and Myovision, written by Wen and Campbell, can expedite these analyses, however both still require extensive user interaction [47], [48]. Both software programs require many manual inputs, extensive human supervision, and are unable to batch process images due to this manual input. Both software programs are also interactive GUIs, at times requiring the user to move a slider bar to threshold an image, thereby introducing user bias. Additionally, by presenting their muscle analysis software programs as GUIs, these programs make it difficult to alter the program to perform other desired analyses. While both software programs are faster than a manual segmentation or count, they still require roughly five minutes per image to segment. Lacking the ability to batch process images significantly inhibits analysis in large experimental studies, usually producing several hundred images for analysis. The novel skeletal muscle fiber segmentation algorithm presented in chapter 3 seeks to remedy these limitations.

2.4.1 Overview of image segmentation techniques

Image segmentation is a technique that partitions an image into multiple regions of interest (ROI). In general segmentation techniques can be classified into four types [49]:

1. Thresholding (Pixel-based segmentation), is the simplest method of segmentation, in which regions are extracted from an imaged based upon the intensity of each pixels color [50].

2. Edge-based segmentation, searches for edges in the image, using either the gradient and/or the Hessian of the image to define contours. This technique can be used to detect changes in color or texture, and its most common method is edge-detection [51].
3. Region-based segmentation, looks at relationships between connected pixels and classifies areas based upon common characteristics to homogeneous groups of pixels. The most commonly used techniques are region growing and the watershed algorithm [52].
4. Model-based segmentation, assigns labels to pixels based upon an a priori knowledge of a known object model in the image data [49]. Model-based segmentations imposes constraints on image segmentation, based upon a priori knowledge that the object/objects of interest have a tendency towards a certain shape or color [53].

The segmentation techniques presented here are not comprehensive and are each subject to limitations such as noise and limits on specifying criteria for classification. As a result many dynamic segmentation strategies combine multiple segmentation techniques to analyze complicated image data sets. As such, the algorithm presented in chapter 2 is a dynamic solution that combines the four techniques listed above.

Chapter 3

Semi-automatic muscle image quantification algorithm

Skeletal muscle is a highly plastic tissue that undergoes adaptation in response to a variety of external stimuli, including disease, exercise, and injury. The most commonly used metric to quantify muscle adaptation is muscle fiber size. Muscle fibers hypertrophy in response to exercise or resistance training, and atrophy as a response to disuse, disease, or injury. As such, experimental studies evaluating muscle injury or regeneration often seek to measure muscle fiber size using fixed muscle tissue cross-sections and histological assessments. Fiber outlines are often visualized using laminin immunostaining, and may also be visualized using hematoxylin and eosin staining. Using histology, muscle fiber cross-section areas, fiber type, fiber geometries, and number of centrally nucleated fibers are all commonly quantified.

While staining allows for the visualization of muscle fiber boundaries, quantification of fiber cross-sectional areas (segmentation) is often performed by manually outlining the boundaries of each fiber within a cross-section (Figure 3.1). This process is extraordinarily time-consuming for scientists, and its accuracy is also limited by the scientists' own manual dexterity. Image quantification that requires extensive human input slows the progress of experimental analysis and also introduces the possibility for user bias.

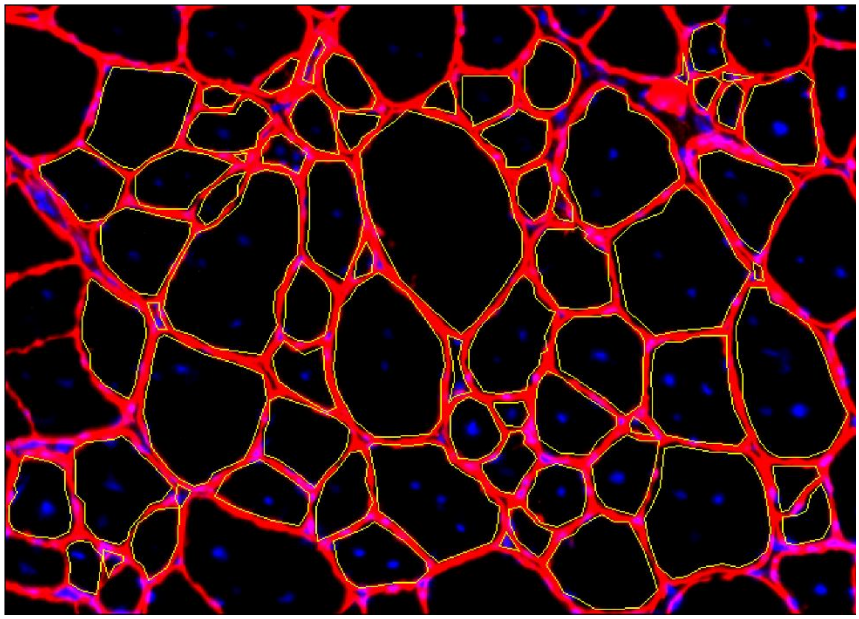

Figure 3.1: Example of Manual Image Segmentation. Confocal image of Laminin-2α and DAPI stained tibialis anterior muscle cross section from *mdx* mouse. Fiber boundaries are red (Laminin-2α), nuclei are blue (DAPI), and the manual image segmentation is yellow (outlined by hand using ImageJ).

Image processing software programs that can expedite muscle histological analysis will greatly accelerate experimental studies of muscle plasticity. While there are several software programs available to perform muscle fiber segmentation, they are expensive, do not allow batch processing, and require considerable manual thresholding adjustment during image processing [47], [48]. Automating muscle histology analysis makes it feasible to efficiently process data from large experimental studies as well as process whole muscle cross-sections, thereby reducing the chance of variability when only a portion of the image is manually segmented. Furthermore, algorithmic determination of muscle fiber cross-sectional-areas reduces variability due to manual dexterity and the possibility of user bias. The purpose of this study was to develop an automatic skeletal muscle image processing software, capable of whole muscle cross-section analysis, and validate the program against

a standard muscle histological manual analysis and two open-sourced currently available skeletal muscle analysis software programs.

3.1 Experimental data collection

The images used for estimating algorithm accuracy were obtained during previous studies of both wild-type and dystrophic mouse tibialis anterior, soleus, and extensor digitorum longus (edl) muscle tissues. No mice were sacrificed specifically for the development or validation of this software. 10 μm thick cryosections of cross-sections of mouse muscle were fixed in 4% PFA, permeabilized with 0.3% triton as needed, blocked with 10% serum, and incubated with Laminin-2-α antibody to define fiber sarcolemmal membranes. Soleus and edl muscles were incubated with the fluorescent dye procion orange before sectioning to assess the algorithms accuracy in determining fiber procion orange dye uptake. Damaged muscle fibers that uptake procion orange dye through leaky muscle fiber sarcolemna is often used as an index of membrane damage. Therefore quantifying the uptake of procion orange dye was of interest. Images were taken of whole muscle cross sections of the soleus and edl muscles, and at 20x for the tibialis anterior muscles.

3.2 Segmentation algorithm design

The software interface flows as follows. Initially, the user inputs the location of the images, and the desired outputs of the algorithm are also specified by the user. While fiber areas are output automatically into a Matlab structure file, optional outputs include spatial statistics for each fiber, number of central nuclei per fiber, presence or absence of procion orange dye within each muscle fiber, and images of the final image segmentation. Procion

orange dye uptake is a common histological measure used as an index of membrane damage as dye is only taken in by muscle fibers with leaky or damaged fiber membranes. The user also defines the object channel that muscle fiber membranes, nuclei, and procion orange dye were imaged using (for example green channel for fiber membranes, red channel for procion orange dye, blue channel for nuclei, etc…). The pixel size in μm/pixel can also be optionally set before image processing begins. Once these initial parameters are set the object channel with the muscle fibers is selected and a mask image is created. To improve contrast within the mask, contrast limited adaptive histogram equalization is applied and the image is binarized using a global threshold determined using Otsu's method [54] (Figure 3.2). An active contour algorithm with 10 iterations was then applied to the original image, using the mask as a guide. 10 iterations were used to create the initial segmentation and to reduce computational complexity. Following the active contour algorithm, the watershed transformation was applied to determine fiber images. The watershed transform can lead to errors in segmentation due to noise within an image. Therefore, prior to the transformation, the image was smoothed to suppress local minima below a specific threshold. Following the watershed transformation, the active contour algorithm was applied once more, with a total of 100 iterations to produce the final image segmentation. 100 iterations were used to produce a smoother final segmentation. Following this segmentation, incomplete muscle fibers at the borders of the image are detected by determining the muscle fibers that are not completely bounded by ECM and excluded from further analysis. An image of the final segmentation is then produced for a visual check (Figure 3.2).

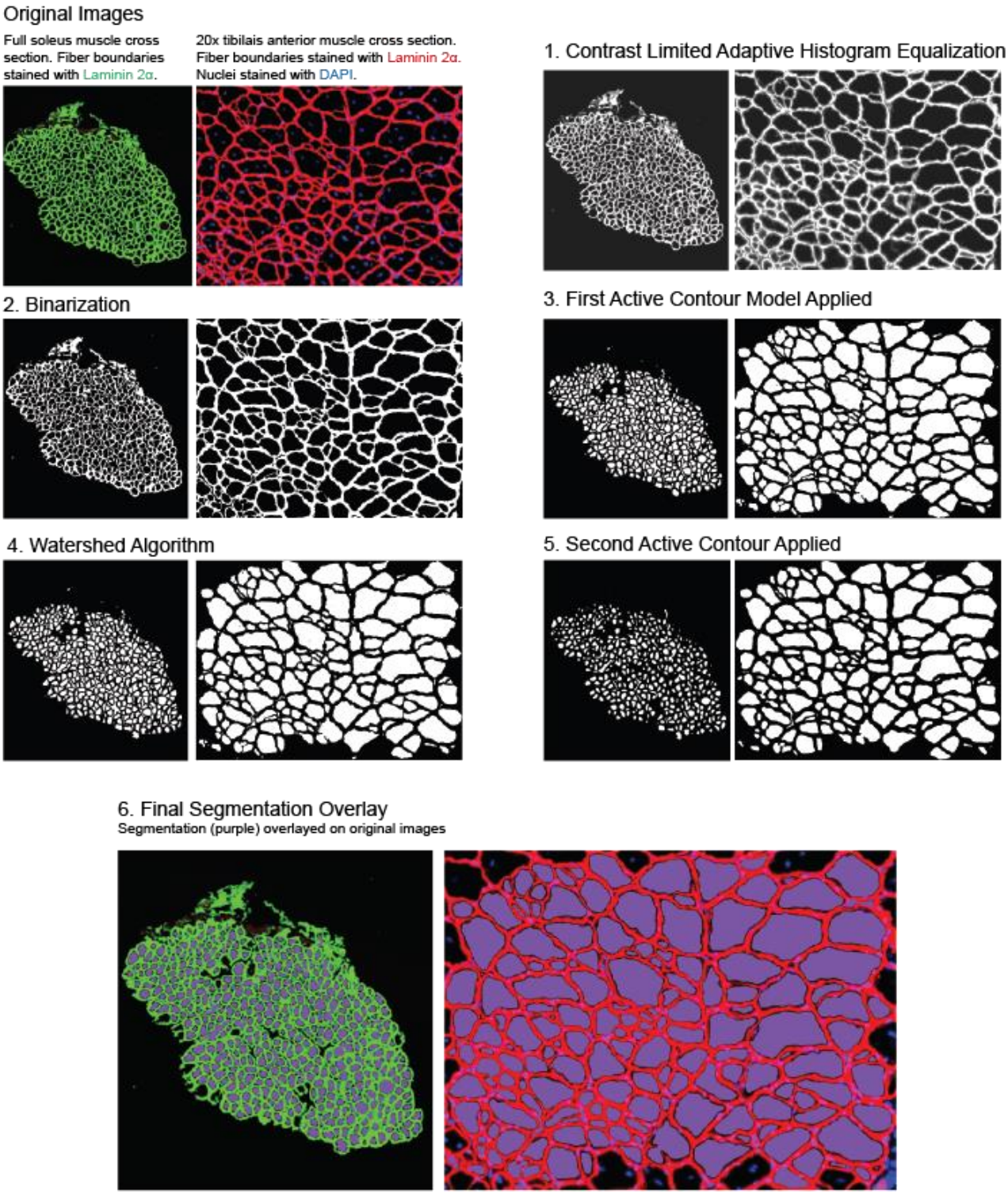

Figure 3.2: Image Segmentation Algorithm Workflow. Major steps in the muscle fiber detection and segmentation algorithm and example segmentations for both 20x and full muscle cross section images.

Following segmentation, spatial statistics of the muscle fibers can also be gathered. Area, perimeter length, centroid, minimum ferret, convexity, extent, shape factor, eccentricity, and deviation properties can be obtained for each fiber (Figure 3.4). To determine centrally nucleated fibers, k-nearest neighbor color clustering algorithm is then used to determine the number of outer or central nuclei within each fiber (Figure 3.3).

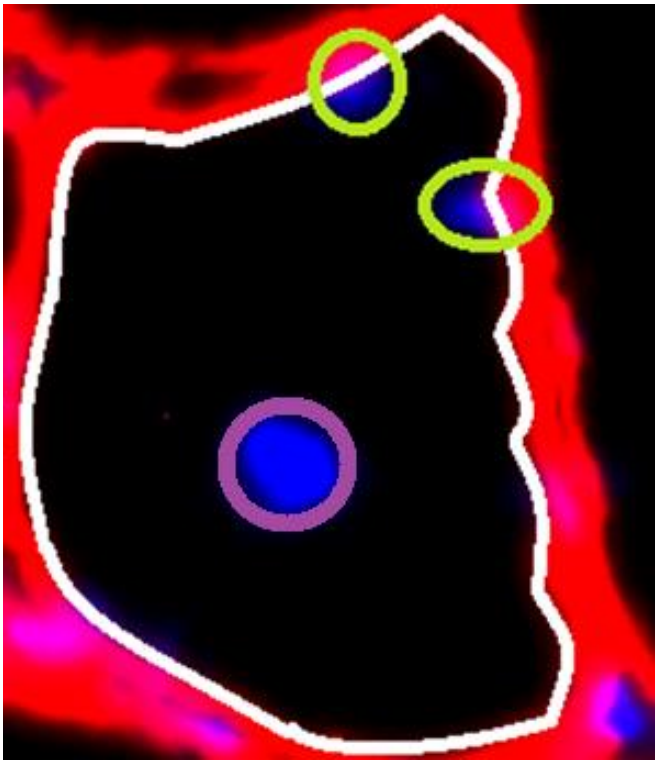

Figure 3.3: Determination of central and outer nuclei in one representative muscle fiber. Representation of K-nearest neighbor color segmentation algorithm to determine central and outer nuclei for one representative muscle fiber. Muscle fiber boundaries are shown in white, central nuclei outlined in purple, and outer nuclei outlined in green.

Another optional feature of the algorithm is the identification of muscle fibers with the presence of procion orange dye inside the sarcolemmal fiber membrane. If this feature is desired, the object channel used to image procion orange dye is isolated, thresholded, and fibers wherein dye is above fifty percent of the area content are identified as positive for procion orange dye. While fifty percent dye area content is the default percentage to

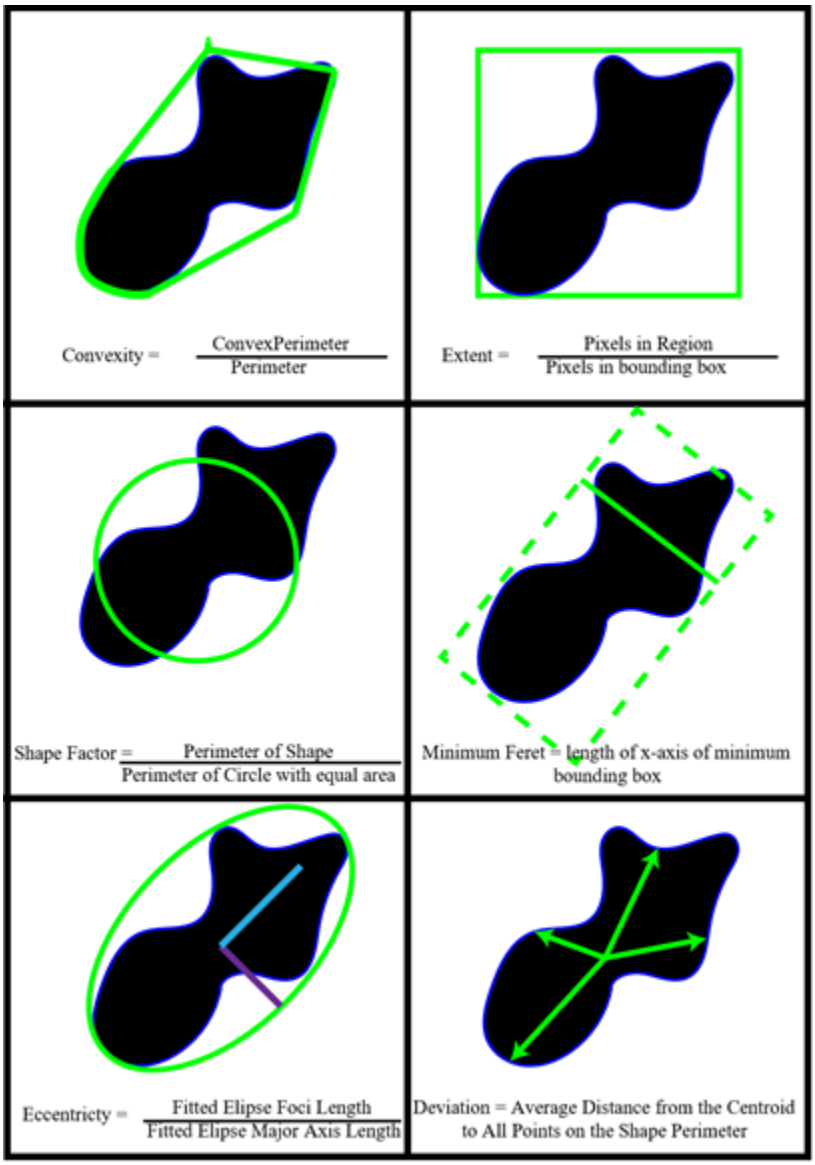

Figure 3.4: Spatial Statistics for each muscle fiber. Convexity, extent, shape factor, minimum ferret, eccentricity, and deviation can be optionally found for each segmented muscle fiber.

identify fibers positive for procion orange dye, this number can be adjusted manually before segmentation begins (Figure 3.5). Additionally, an optional feature of the algorithm at this stage removes the outer two layers of muscle fibers for analysis, as this is a common procedure to eliminate the bias due to sectioning errors at the edge of a whole muscle-cross-section. The outer two layers of fibers can be removed by finding the center of each

fiber within the image, and iteratively removing the fibers with centroids at the outer edge of the whole muscle cross-section.

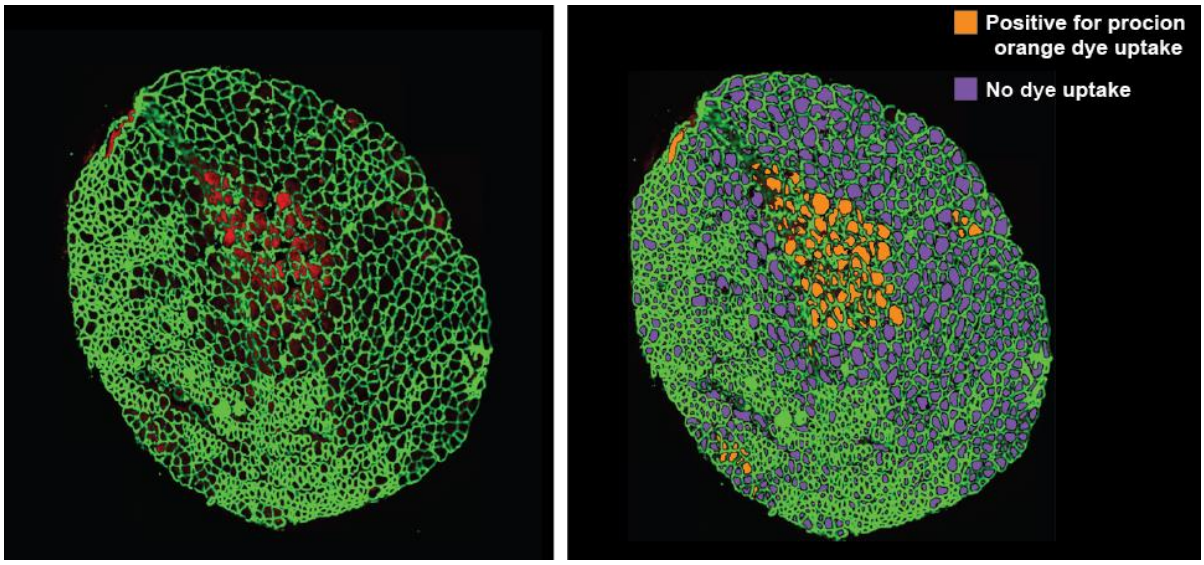

Figure 3.5: Example of identification and segmentation of muscle fibers containing procion orange dye. Original image shown at left and segmented image shown at right.

3.3 Comparison of segmentation performance

The accuracy of muscle fiber counts and muscle fiber areas was determined by comparison with manual count and manual segmentation. Two open-sourced software applications, Myovision and SMASH, were also downloaded to evaluate the current algorithm's accuracy to the currently available open-source techniques. Detailed descriptions of both the SMASH and Myovision software programs have been published [47], [48]. To compare algorithm segmentation accuracy, we used the dice similarity coefficient. The dice similarity coefficient is a statistical validation metric to evaluate the performance of automated segmentations, comparing to a manual segmentation set as a gold standard (Figure 3.6). The dice similarity coefficient, also called the overlap index, is the most commonly used metric in validating medical segmentations [55]. When

calculating the dice similarity coefficient, two binary segmentations are needed, one representing the "ground truth" image and the other the automated segmentation that is being evaluated. Euclidean distance and the following equation are used to calculate the dice similarity coefficient between segmentations A (Ground truth) and B (automatic).

$$\text{Dice Coefficient} = \frac{2(A \cap B)}{A + B} \tag{8}$$

Dice coefficients range from 0 to 1, with 1 being a perfect segmentation (Figure 3.6). Any segmentation above a 0.75 dice similarity coefficient, is considered to be a good segmentation [56].

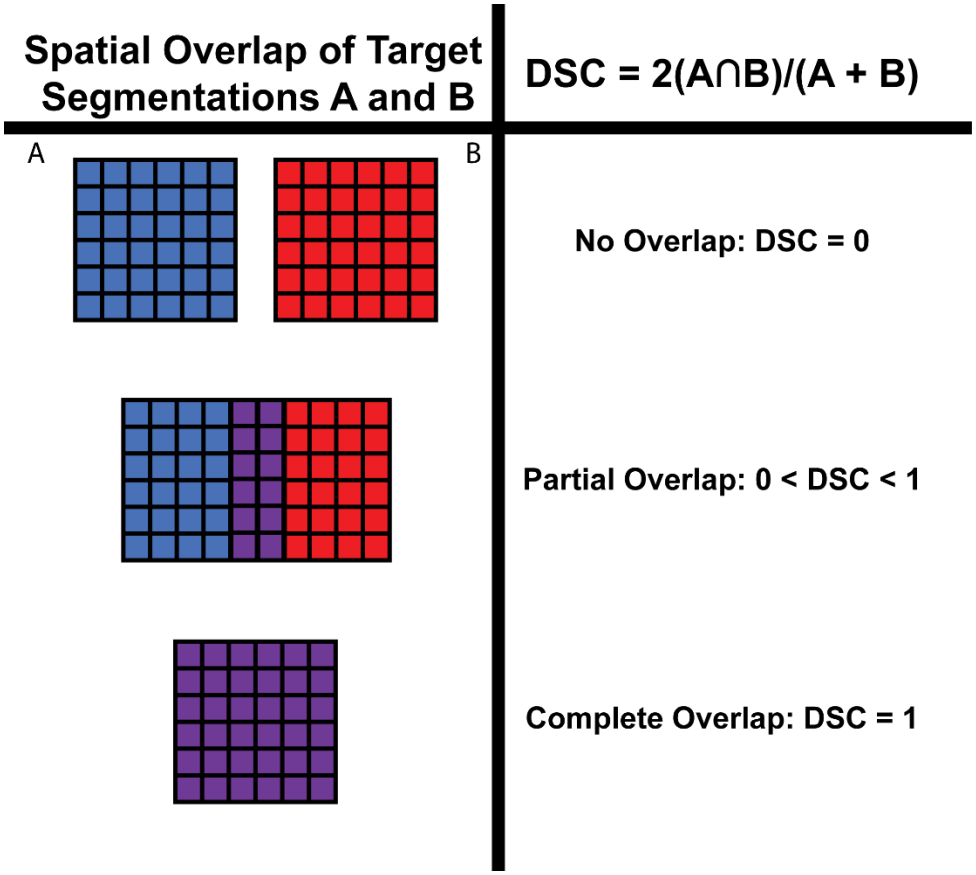

Figure 3.6: Schematic of Dice Similarity Coefficient. A representative diagram comparing two segmentations, A and B, using the dice similarity coefficient. The dice similarity coefficients compares segmentations on a scale of 0 to 1, with 0 representing no overlap in segmentation, and 1 representing segmentations that are identical.

3.3.1 Methods for Validating the Segmentation Algorithm

The algorithm was validated in two ways:

1. *Mdx* and *wt* images (20x) of tibialis anterior murine muscle cross-sections were manually segmented using the outline tool of ImageJ (n = 13). The time to manually segment each image was recorded. The manual segmentation was then compared to segmentations produced by the algorithm presented above, Smash open-source software, and Myovision open source software using the dice similarity coefficient. These segmentations were timed as well. Segmentation performance was evaluated using the dice similarity coefficient to compare to the manual segmentation set as the gold standard. Segmentation time was also evaluated and compared.
2. Whole muscle cross sectional images of *mdx* and wild-type (*wt)* edl and soleus muscles (n = 14) were evaluated by a team of five trained muscle physiologists. The samples were stained with Laminin-2α to visualize muscle fiber boundaries and incubated with procion orange dye to visualize dye uptake. As each whole muscle cross-section contains several hundred muscle fibers, a manual segmentation was not performed due to time constraints. Instead, each technician counted the total number of muscle fibers present in each sample, as well as the total number of fibers with procion orange dye uptake, to evaluate the accuracy of that feature of the new software. The algorithms total number of fibers and percent of fibers with procion orange dye uptake were then compared back to the manual counts to evaluate accuracy.

3.3.2 Results of Segmentation Algorithm Validation

The algorithm segmentations of the 20x tibialis anterior *wt* images displayed a significant increase in segmentation quality (as compared to the manual segmentation using the dice similarity coefficient) compared to those produced using Smash software (Figure, 3.7, $p < 0.05$) [47]. Furthermore, the algorithm segmentations were significantly better than both Smash and Myovision software programs on the *DMD* 20x tibialis anterior muscle images software (Figure 3.7, $p < 0.05$) [47], [48]. DMD muscle is difficult to segment due to an increase in interstitial space between fibers, leading to over classification of extracellular material as muscle. Additionally, the fibers are less uniform in shape, leading to challenges in image processing. While the all segmentations produced by the new algorithm, Smash, and

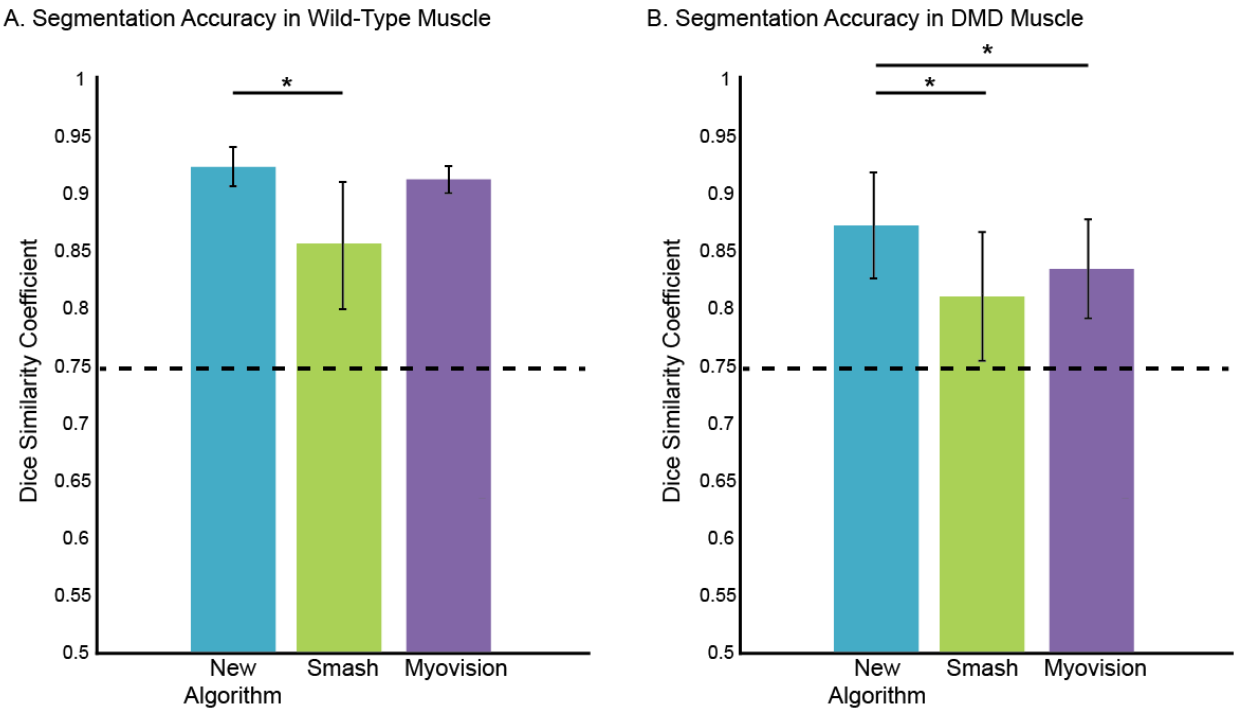

Figure 3.7: Accuracy of Segmentation of Dystrophic and Healthy Muscle. Segmentation accuracy was compared using the dice similarity coefficient on groups of Wild-Type (n = 6) and dystrophic (n = 7) cross sections. Error bars represent the standard deviation from the mean. Significance was calculated using ANOVA and Tukey post-hoc tests at the p = 0.05 level.

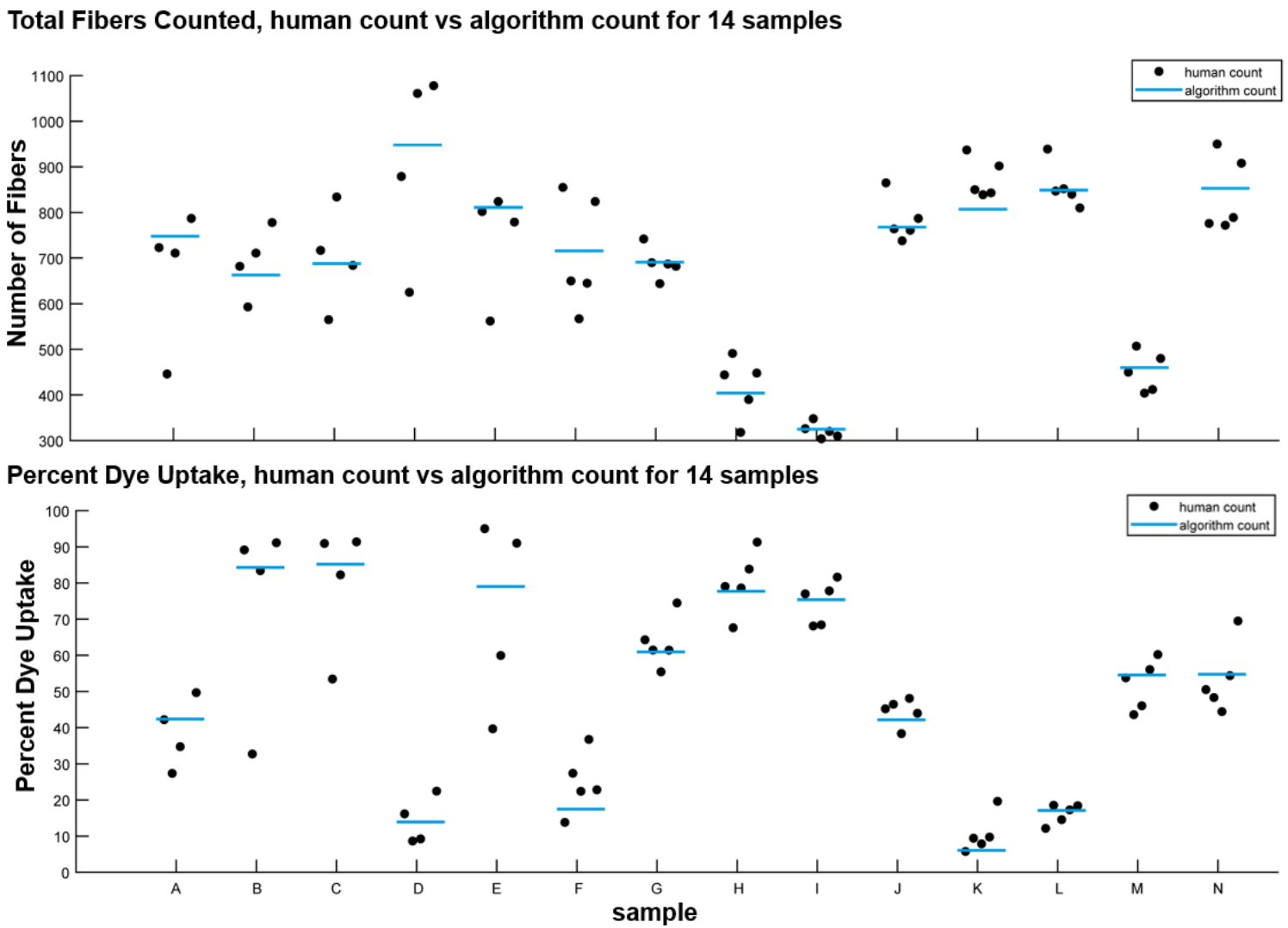

Figure 3.8: Comparison of algorithm segmentation to a human manual count. A team of five trained technicians performed a manual muscle fiber count on 14 whole muscle cross-sections. Muscle fibers positive for procion orange dye uptake were also counted. The number of total fibers counted and the percent of fibers displaying dye uptake was then calculated using the algorithm and compared to the manual counts.

Myovision were above the standard 0.75 cutoff to mark a "good" segmentation, the new algorithm dice similarity coefficient average across all samples was 0.91, which is indicative of a high quality segmentation across all samples.

The whole muscle cross-section image analysis indicates that the algorithm compares favorably with human measurements conducting a whole-muscle cross-section count. As shown in Figure 3.8, there is considerable variability among humans conducting a manual count of muscle fibers in muscle cross-sections consisting of several hundred fibers, with counts varying as much as 75 percent between the minimum and maximum human counts. Across 14 samples, there was an average of 3.7 percent error between the algorithm muscle fiber count and the manual human count (Figure 3.8). Furthermore, the results indicate that the algorithm counting of procion orange dye uptake by individual muscle fibers compares favorably with a human manual count. Across 14 samples there was an average of 2.1 percent error in the counting of muscle fibers out of the total with procion orange dye uptake (Figure 3.8).

3.4 Operating time discussion

Operating time was evaluated by timing the manual segmentation, the open source software segmentations, and the algorithm segmentation for each image. As both SMASH and Myovision open source software require human involvement in the setting of parameters for segmentation and are unable to batch process images, they had significantly higher average operating times per image. The algorithm significantly decreases segmentation time compared to the manual segmentation ($p < 0.001$). Furthermore, the algorithm significantly decreases segmentation time compared to both the Smash and Myovision software programs ($p < 0.05$, Figure 3.9). As the algorithm both increases the

accuracy of muscle image segmentation and is more efficient in its use of time, the algorithm is a much needed improvement over previously available methods.

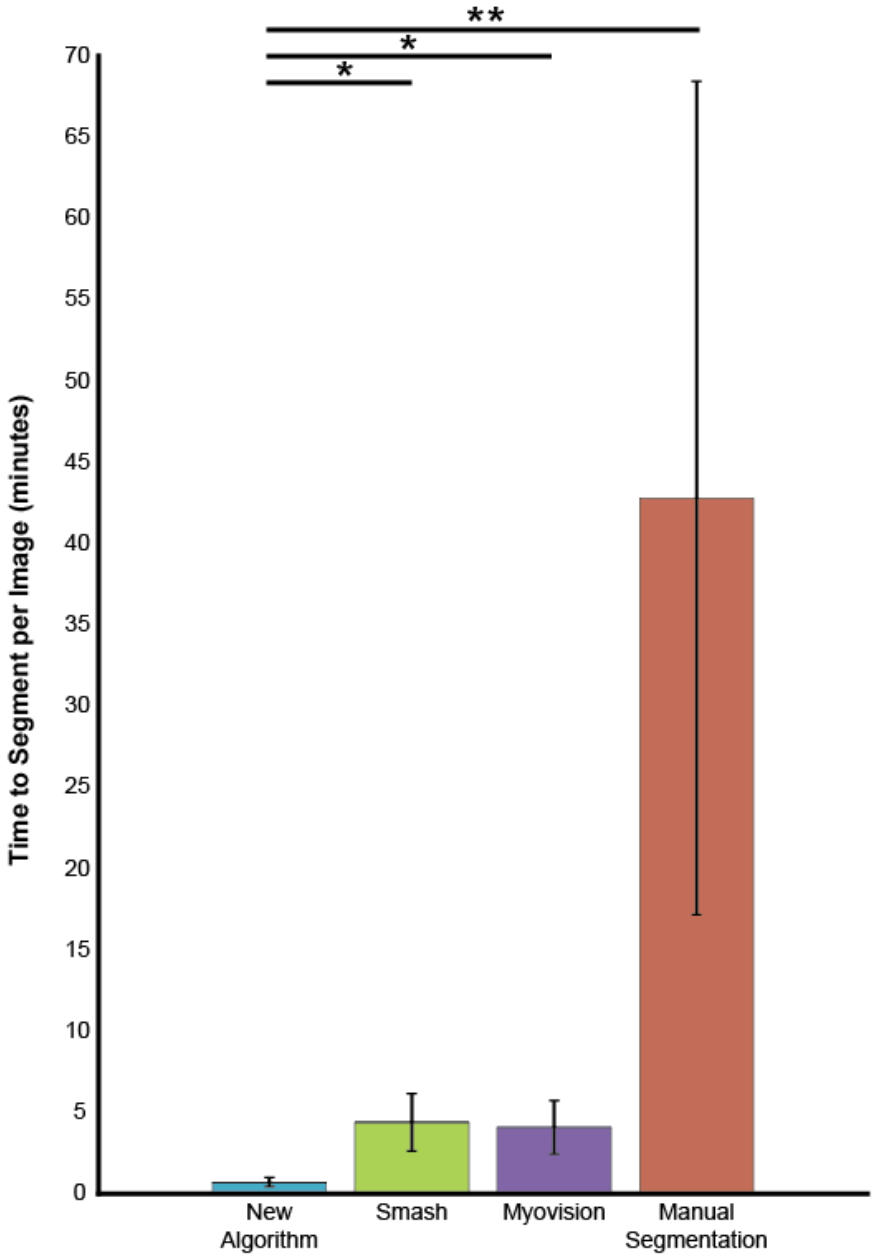

Figure 3.9: Efficiency of Image Segmentation Algorithm. 13 20x tibialis anterior images were segmented using the new algorithm, open-source software programs Smash and Myovision, and manually segmented using ImageJ. Segmentations were timed and compared. Error bars represent standard deviation from the mean. Significance was calculated using ANOVA and Tukey post-hoc tests at the $p = 0.05$ level. * indicates significance at the $p<0.05$ level, ** indicates significant at the $p <0.001$ level.

3.5 Application of algorithm to a case study on contraction-induced injury in Duchenne muscular dystrophy

Following validation of the algorithm, it was applied to study contraction-induced injury in Duchenne muscular dystrophy (DMD). In DMD it remains unclear why some lower limb muscles degenerate at a different pace than other muscles, despite the fact that dystrophin is absent or deficient in all lower limb muscles. Eccentric contraction movements are one of the most damaging activities to dystrophic muscle. All lower limb muscles are exposed to eccentric contraction movements during walking, albeit at differing muscle-dependent levels. Therefore, it has been hypothesized that the selective degeneration of muscles in DMD is due to differing levels of eccentric contraction during walking. However, it has been difficult to generalize animal studies to humans as muscle function during gait varies greatly between biped humans and quadruped mouse models [57].

While previous work has demonstrated that *mdx* mouse muscles are more susceptible to contraction-induced injury than wild-type muscles, many of these studies imposed arbitrary contraction or injury conditions that do not replicate the function of lower-limb muscles during movement [58]–[60]. Therefore, a protocol mimicking the conditions that occur during human movements was developed to test the mouse muscles under more human-like contraction conditions. Healthy human soleus and edl force and length change profiles during a single walking step were simulated using OpenSim. Time dependent force and length change profiles form the simulation were then programmed using an Aurura Scientific Inc 300B dual mode servo motor to create a gait-mimicking eccentric contraction protocol. Wild-type and *mdx* mice at ages 5-7 weeks were euthanized, muscles were dissected, and left lower limb soleus and edl muscles were fixed and exposed to the gait mimicking protocol. The gait mimicking protocol was run for either 200 or 25

steps. Right lower limb muscles were kept as a control and not exposed to the protocol. All muscles were then mounted in OCT and stored at -80°C for subsequent sectioning. Muscles were then bathed in procion orange dye to determine sarcolemmal damage and laminin-2α to visualize fiber boundaries. Dye uptake was quantified using the previously validated algorithm.

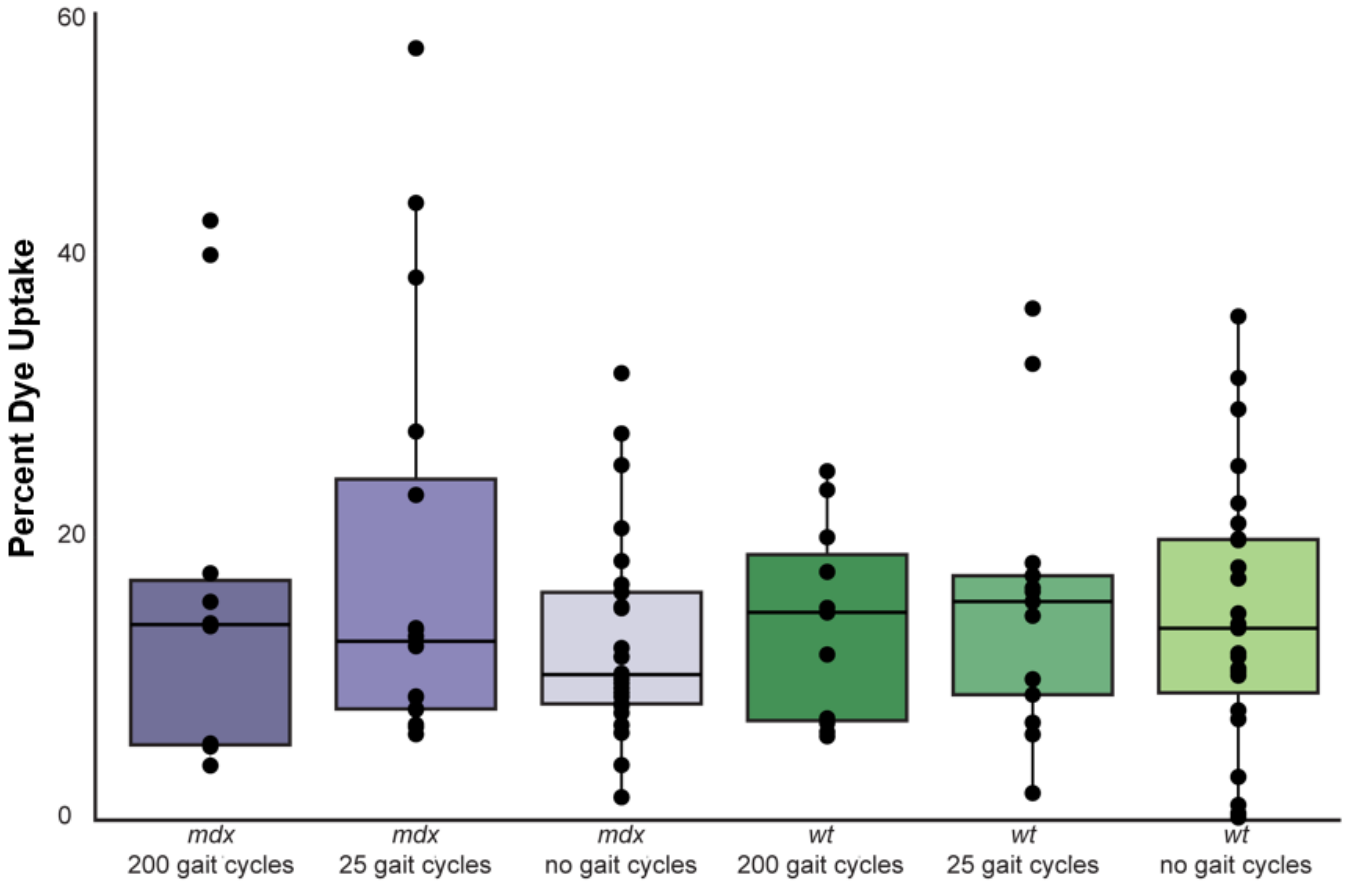

Figure 3.10: Effect of Gait Protocol on Procion Orange Dye Uptake in *mdx* and *wt* Muscle. Horizontal bars represent the median, lower and upper box boundaries represent the first and third quartiles, lines represent 1.5 times the interquartile range, dots represent individual muscle cross-sections. Based upon a 2-way ANOVA there are no significant differences in the means of all groups.

Dye uptake was variable across *mdx* and *wt* muscles. While there were no significant differences between groups (2 – way anova, $p > 0.05$, $n = 102$), the *mdx* muscles exposed to the gait-injury protocol had the most variability in dye uptake, ranging from 4 percent of fibers with procion orange dye uptake, to 56 percent of fibers with dye uptake (Figure 3.10). There were also no significant differences in dye uptake, regardless of the number of gait cycles the muscle underwent. Furthermore, there were different trends in dye uptake between the soleus and edl muscles (Figure 3.11). Overall the majority of *mdx* soleus muscles showed less dye uptake than the wild-type soleus muscles. However, there were 4 soleus muscle samples that were clearly outliers and were several standard deviations above the mean for the mdx-gait injury protocol group. Across EDL muscles there were no significant differences in the means based upon either genotype or gait cycle. However, the mdx-injury group again showed the greatest variability of all groups.

The heteroscedasticity in muscle sarcolemmal damage in response to a gait-mimicking eccentric contraction injury protocol leads to more questions on the effect of muscle microstructure on damage susceptibility. Are some muscles more predisposed to damage than others, regardless of the presence or absence of dystrophin? If so, is that predisposition a function of muscle microstructure or other cellular processes? Can we use microstructures to predict damage? Were there subject to subject differences in activity prior to testing that lead to a greater muscle damage susceptibility? Previous micromechanical FE modeling work has shown that microstructural elements such as adipose infiltration do not effect membrane strain, and a similar approach could be used to determine if muscle microstructures are predisposed to damage [4].

The image processing algorithm presented here provides a new tool for muscle analysis and for determining muscle microstructural properties in a time-efficient manner. The application of this algorithm to a case study investigating Duchenne muscular dystrophy

allowed for the analysis of 102 whole muscle cross-sections, saving months of time that would have been required for the manual analysis.

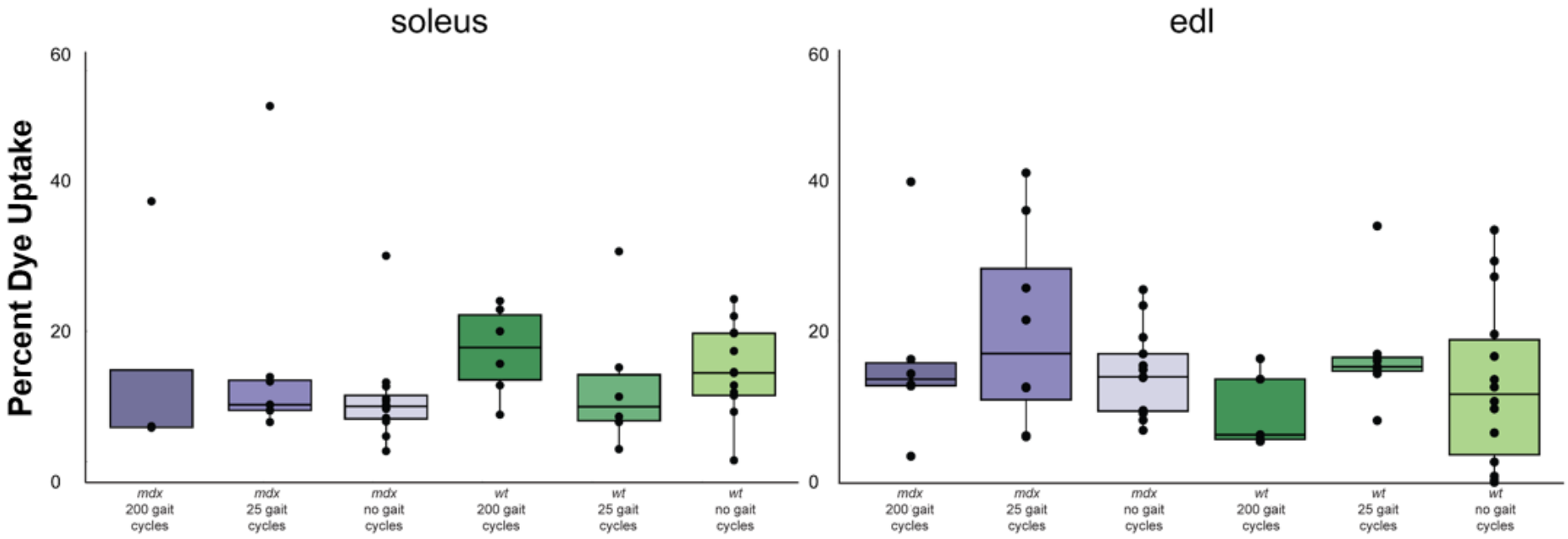

Figure 3.11: Effect of Gait Mimicking Protocol on Procion Orange Dye Uptake in Soleus and EDL Muscles. Horizontal bars represent the median, lower and upper box boundaries represent the first and third quartiles, lines represent 1.5 times the interquartile range, dots represent individual muscle cross-sections. Based upon a 2-way ANOVA there are no significant differences in the means of all groups.

Chapter 4

Modeling the Effect of Muscle Microstructure on Damage Susceptibility in Duchenne muscular dystrophy

Recently, FE models of skeletal muscle microstructure have been used to understand how DMD-related changes in muscle influence the susceptibility for muscle to induce damage during contraction [4]. In section 3.5 we found that damage susceptibility in both *DMD* and *wt* muscle varies greatly between muscles and there were no significant differences in muscle damage before and after gait-mimicking eccentric contraction injury protocols in both dystrophic and wild-type muscle. Therefore, in order to better understand how muscle microstructure variation effects damage susceptibility, we applied the aforementioned micromechanical modelling technique to a selection of muscle cross sections previously analysed in section 3.5.

4.1 Methods

4.1.1 Conversion of image to finite element model

Fifteen cross-sectional muscle cross-sectional images were selected to convert to finite element models. Images were selected of both healthy and dystrophic muscle, as well as muscles that underwent the 200 cycle gait protocol and no gait protocol. Selection criteria for images required that images were of complete cross-sections with no sectioning errors. The segmentation algorithm was applied to each cross-sectional image to identify

muscle fibers, and the outer border of the cross-section (Figure 4.1). Each material element from the segmentation was then mapped onto an initialized finite element mesh to represent the whole-muscle cross-section. Each pixel was mapped to one hexahedral mesh element. Finite element meshes consisted of approximately 350,000 elements, and were one element thick. Previously published micromechanical modeling work has determined that calculated shear moduli and strains are within 0.5% of each other when geometries are modeled with a one element thick mesh or a three element thick mesh [4]. Therefore, to reduce computational time, a one-element-thick mesh was used.

Boundary conditions were assigned to the finite element models to prescribe a simple shear deformation that is experienced during an eccentric muscle contraction. As muscle fiber force is transmitted laterally through the shearing of the endomysium, the prescribed shear deformation represents the shear displacement of muscle fibers and relative to each other. To prescribe the shear deformation, the elements on the -x face were constrained in all directions, and the elements on the opposing face (+x) were displaced in the -z direction creating a shear displacement in the xz direction (Figure 4.3). All elements were constrained in the x and y directions. Max displacement was set at one-third of the width of the muscle cross-sections widest point in the x direction. Simulations were also run fixing the (-y) face, constraining the (+y) face, and setting displacements to one-third the width of the widest point of the cross-section in the y direction, creating shear displacements in the yz direction. Outputs from both simulations were then averaged before calculating strains.

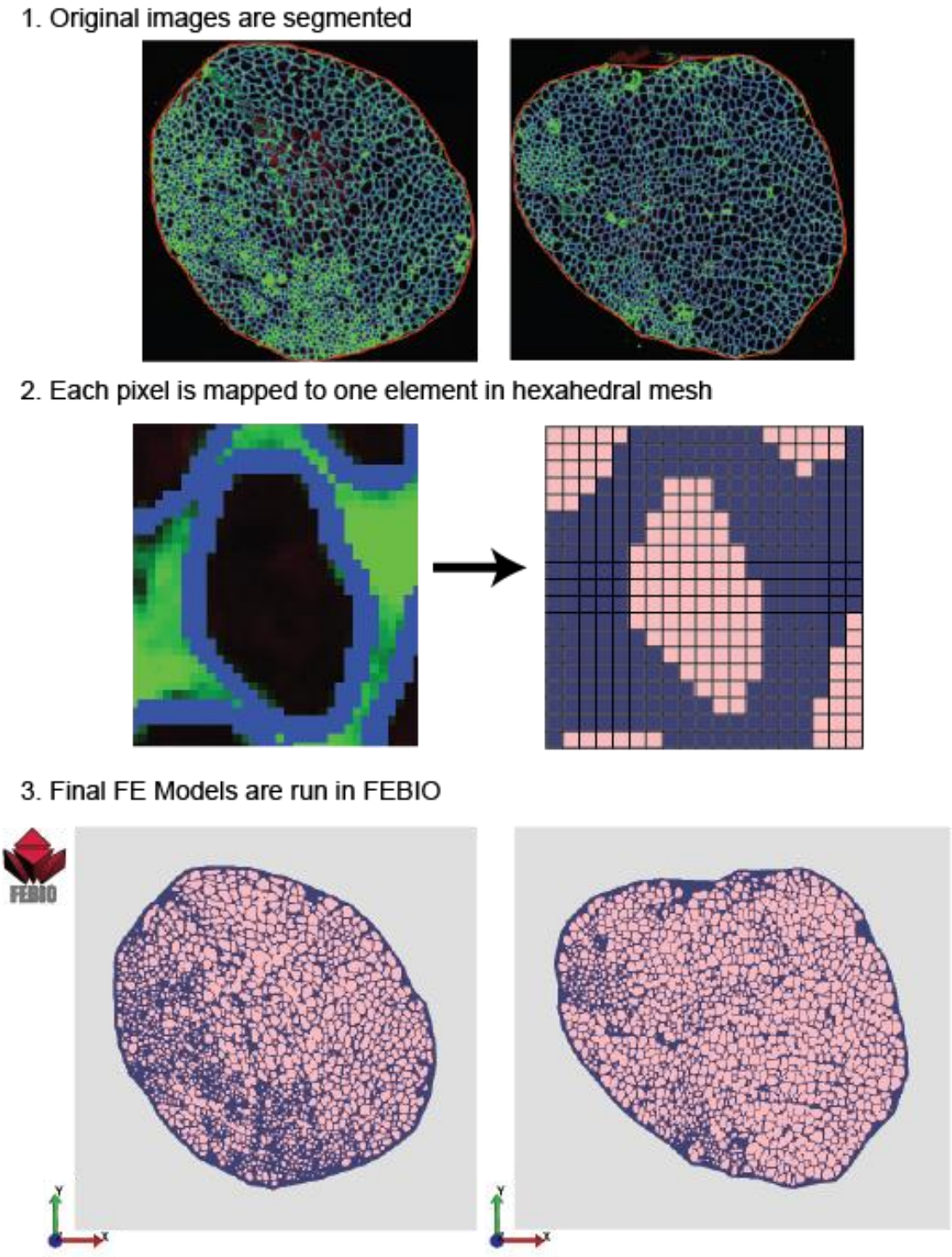

Figure 4.1: Image to Finite Element Model Workflow for Two Representative Images. Muscle fiber segmentations are outlined in blue, with whole muscle boundaries outlined in red. A representative muscle fiber is mapped to a hexahedral mesh where pink indicates the muscle fiber and blue the extracellular material. Two finite element models are shown based upon the initial segmentations.

4.1.2 Transmembrane protein inclusion

The absence of transmembrane proteins in DMD was modeled in FE models based upon dystrophic cross-sections, and alternatively the presence of dystrophin was modeled in the FE models based upon wild-type muscle cross-sections. The transmembrane protein was modeled as a nonlinear elastic spring [4], [61], [62]. All nodes connecting the muscle fibers and extracellular matrix were identified, a node was added at that location, and the two nodes were connected with the nonlinear elastic spring (Figure 4.2). Wild-type muscle was modeled with a spring at one-hundred percent of the muscle fiber – ECM junctions. As the absence of dystrophin in DMD leads to an approximately 80-90% reduction in all components of the dystrophin associated glycoprotein complex (Figure 2.1), a random number generator was used to randomly delete 90% of the springs in the FE models of dystrophic muscle [63].

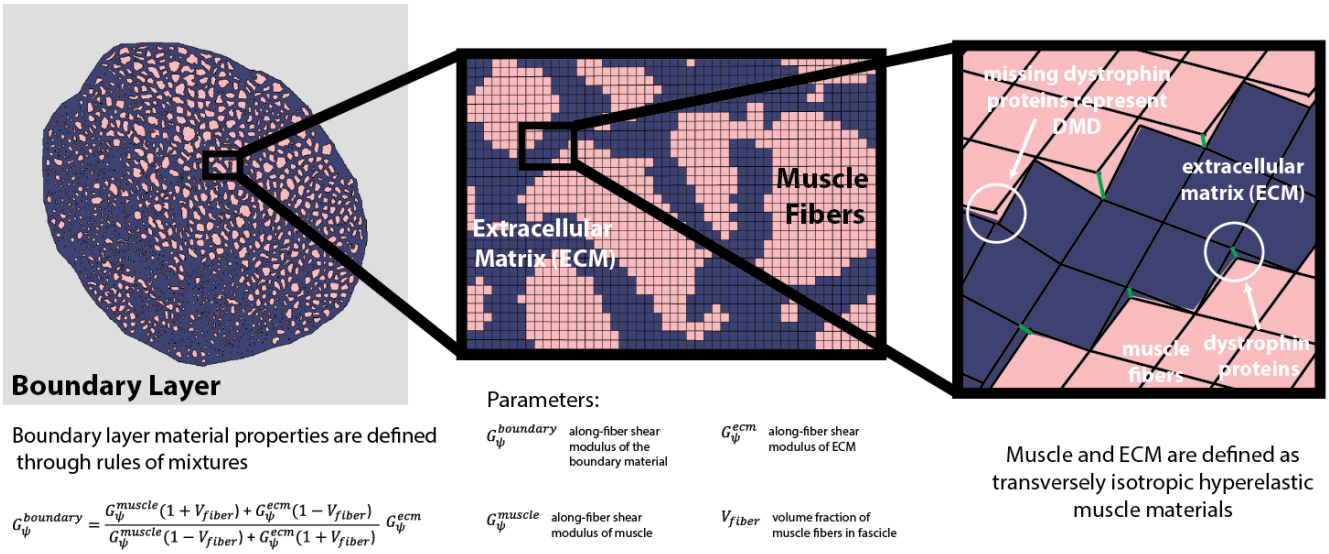

Figure 4.2: Components of finite-element micromechanical model. Image-based geometries were mapped to finite element meshes, and a boundary layer was defined. Nonlinear elastic springs were incorporated into the models to represent both the presence (in wt) and loss (in mdx) of transmembrane proteins

4.1.3 Inclusion of Boundary Material

Building upon the work of Virgilio et al., the muscle cross-sections were surrounded by a boundary layer with pre-allocated properties that were adjusted to simulate the macroscopic shear properties of the muscle cross section [4]. The boundary layer was included to model the irregular boundaries of the muscle cross-section and allow for multiple real muscle cross-section geometries to be modeled. In order to prevent the boundary layer from adversely affecting the model, the material properties of the boundary were adjusted so that its behavior simulated the macroscopic shear properties of the muscle cross section. Using the rule of mixtures, a homogenized macroscopically representative material was used to define the boundary layer. The boundary material's along-fiber shear properties were defined as follows where V_{fiber} is defined as the volume fraction of muscle fibers within the muscle cross-section.

$$G_{\psi}^{boundary} = \frac{G_{\psi}^{muscle}(1 + V_{fiber}) + G_{\psi}^{ECM}(1 - V_{fiber})}{G_{\psi}^{muscle}(1 - V_{fiber}) + G_{\psi}^{ECM}(1 + V_{fiber})} \quad (9)$$

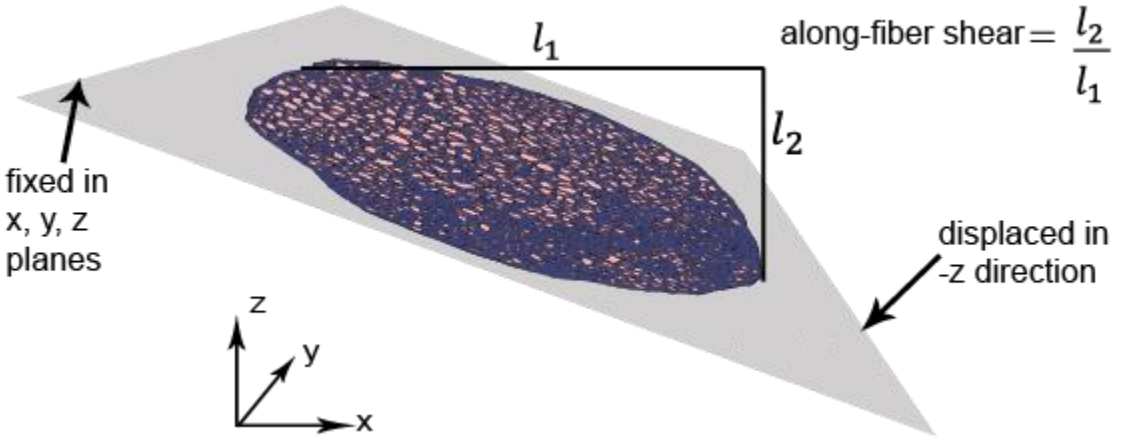

Figure 4.3: Representative finite-element model in shear. Boundary conditions were assigned to the FE models to prescribe a simple shear deformation experienced during eccentric muscle contraction that occur during gait.

4.1.4 Constitutive model and material parameters

The constitutive model and material properties used were as described in section 2.3.2. Although there are few known measurements of the along-fiber shear moduli of muscle and ECM, previous work has shown that the ratio of these shear moduli has an impact on tissue-level properties. This ratio was kept at one in which muscle is 75 times stiffer than the ECM [17].

4.1.5 Determination of Membrane Strain

Simulations were run using the nonlinear finite element analysis software suite, FEbio. Due to the size of the simulations (approximately 350,000 elements) for efficiency simulations were run on an 8 core, 240 GB computing cluster. Average simulation time was 45 minutes, when simulations were run on the computing cluster. Membrane strain was calculated by determining the change in length between fiber and ECM nodes at both the spring locations and the muscle-ECM junctions missing springs, normalized by the displacement of the cross-section. Cross-section displacement was calculated by

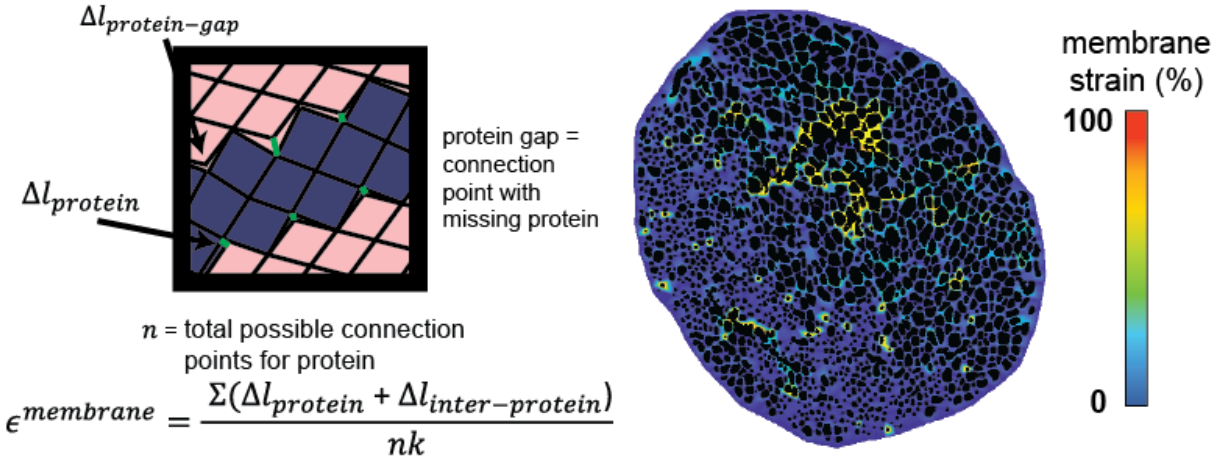

Figure 4.4: Calculation of membrane strain. Membrane strain, a measure of the strain in the proteins and indicative of muscle susceptibility to damage, is calculated after micro-level eccentric contraction simulation

determining displacement in the z direction and dividing by the width of the cross-section. Membrane strains across the entire cross-section were averaged to determine average cross-sectional membrane strain for each sample. Percent dye uptake was calculated for each muscle cross-section by determining the percentage of muscle fibers positive for procion orange dye in the original histological image, and dividing that number by the total number of muscle fibers present in the cross section. The percent procion orange dye uptake served as the experimental index of muscle damage [64].

4.3 Results

There was a positive correlation between FE model average predicted membrane strain and procion orange dye uptake ($p = 0.006$, $R^2 = 0.41$, Figure 4.5A). The results suggest that membrane strain predicted by the micromechanical muscle models are predictive of membrane damage in both healthy and dystrophic muscles. When grouped according to whether the muscle had undergone the gait mimicking protocol (Figure 4.5B,C), the samples that underwent the gait protocol had a smaller correlation coefficient (slope of the linear regression). Meaning that for equal strains, samples that underwent the gait protocol displayed higher dye uptake.

To examine how the microstructure variations affect cross-sectional membrane strain (and thus damage susceptibility), minimum feret's diameters, areas, and shape factors were calculated for each fiber within each cross section. Minimum feret's diameter is the minimum distance of parallel tangents at opposing borders of the muscle fiber and is often used to quantify muscular degeneration in DMD [64]. Shape factor is a dimensionless measure of circularity defined as the perimeter of the muscle fiber divided by the perimeter of a circle with perfect area. Therefore, a perfect circle has a shape factor of 1, and circularity

decreases as shape factor increases from 1. To get holistic measures of each cross-sections microstructure, the average, median, range, and coefficient of variance was found for each of these quantities for each cross-section. Coefficient of variance is defined as the ratio of the standard deviation to the mean. It is a commonly used statistic to measure dispersion of a dataset. The coefficient of variance for the minimum feret's diameter had the most significant impact on FE model membrane strain ($p = 0.0014$, Figure 4.6). Other significant predictors for membrane strain included the average shape factor ($p = 0.02$, Figure 4.6), median fiber area ($p = 0.047$, Figure 4.6), median minimum feret's diameter ($p = 0.049$, Figure 4.6), and the coefficient of variance for muscle fiber size ($p = 0.0042$, Figure 4.6). These predictions are consistent with recent studies determining the impact of muscle fiber size on susceptibility to damage [4], [65].

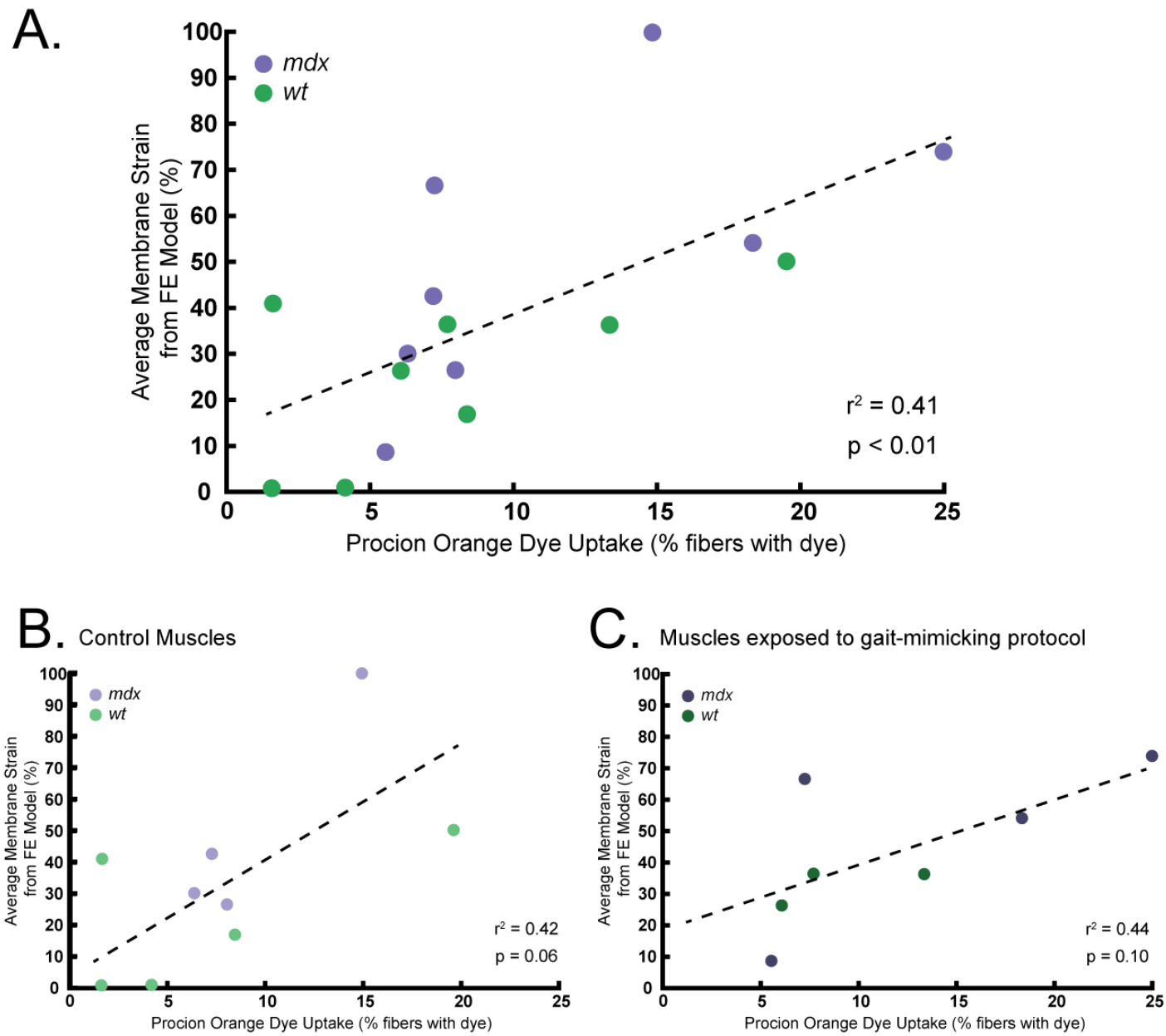

Figure 4.5: Relationship between histological dye uptake, average membrane strain, and exposure to gait mimicking protocol. (A) Correlation between model-derived membrane strain and experimentally measured muscle damage. (B) Correlation between model-derived membrane strain and experimentally measured muscle damage for the subsection of muscles not exposed to the gait-mimicking protocol. (C) Correlation between model-derived membrane strain and experimentally measured muscle damage for the subsection of muscles exposed to the gait-mimicking protocol.

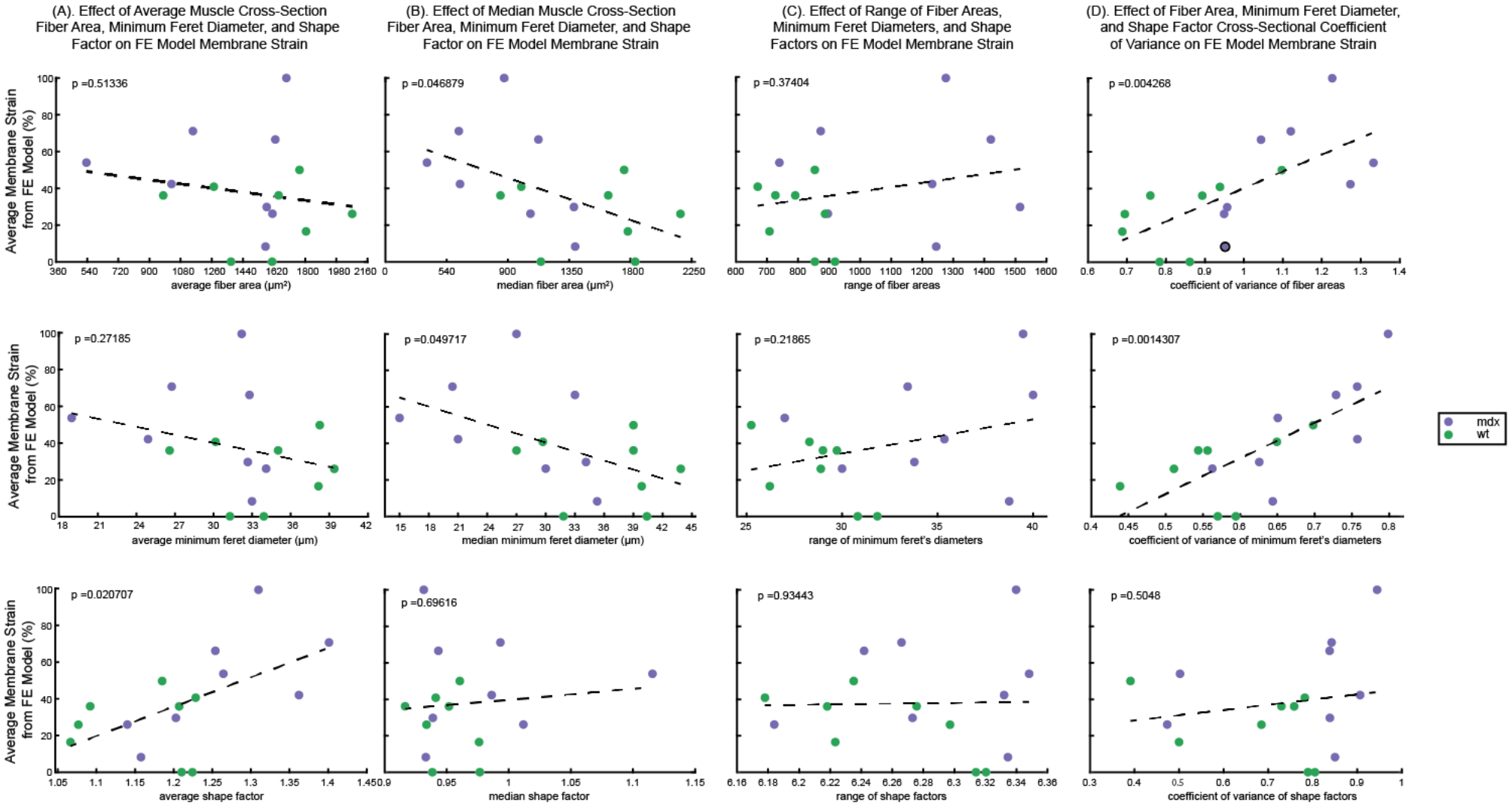

Figure 4.6: Membrane Strain is affected by Cross-Sectional Median Fiber Area, average shape factor, median minimum feret's diameter, fiber area coefficient of variance and shape factor coefficient of variance. Spatial statistics were calculated for each muscle cross-section and compared to the average membrane strain in each cross-section.

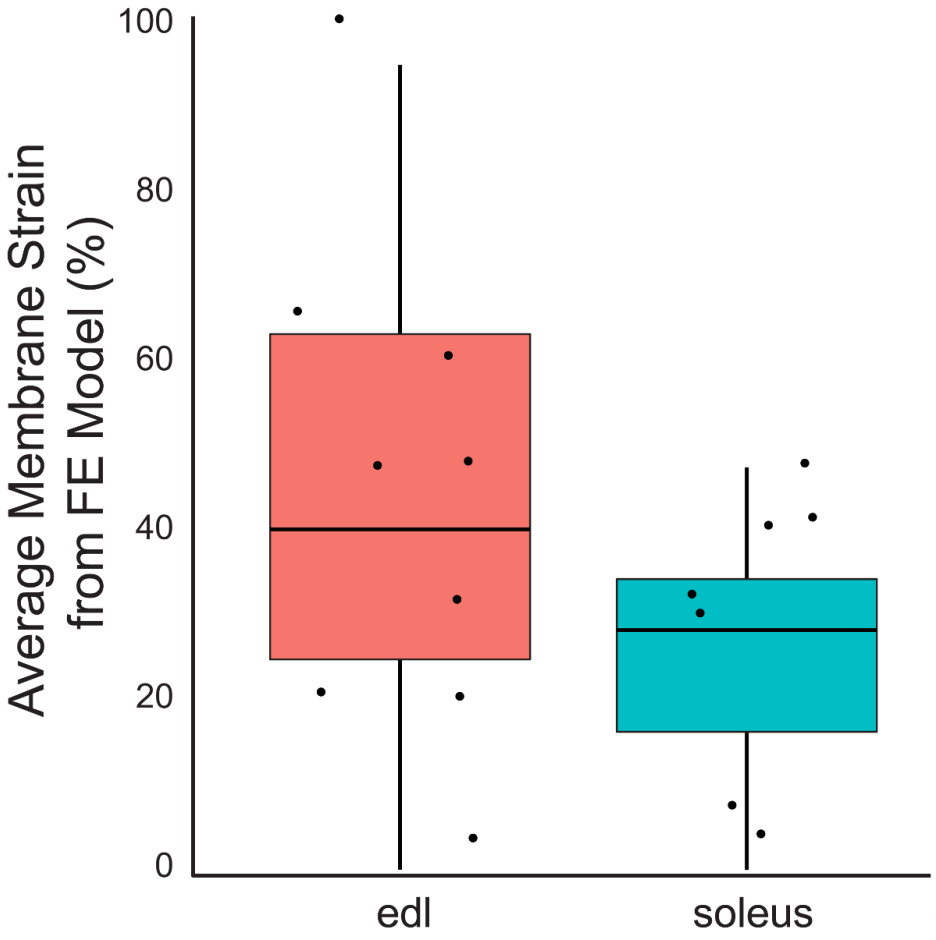

Figure 4.7: EDL cross-sections display greater variability and higher average membrane strains than Soleus cross-sections. Membrane strain was calculated as described in Section 4.1.5. Although there is no significant difference between the means (t-test, $p > 0.05$), the general trend of the EDL muscle displaying greater strains than the soleus, is consistent with findings in the literature.

Additionally, our findings are consistent with literature that shows that the EDL is more susceptible to eccentric contraction-induced damage than the soleus [66], [67] (Figure 4.7) . Previous research has suggested that the EDL is more susceptible to contraction induced damage due having smaller and less rounded fibers in those muscles than in the soleus. Multiple regression analysis was used to test if these microstructural variations significantly predict FE model membrane strain (Table 4.1). The results of the regression indicate that 3 predictors (Muscle, Variance of Minimum Feret's Diameter, and Median Shape

Factor) explain 77 percent of the variance of FE model membrane strain (R^2 = 0.811, F(7,8) = 3.93, p = 0.03692, Table 4.1).

	FE Model Membrane Strain		
Predictors	*Estimates*	*CI*	*p*
(Intercept)	-31.74	-70.41 – 6.92	0.146
Coefficient of Variance – minimum feret's diameter (variance_minferet)	48.49	-9.35 – 106.34	0.139
Muscle type	109.99	-2.18 – 222.16	0.091
Median Shape Factor	31.41	-8.24 – 71.07	0.159
variance_minferet:Muscle	-189.84	-375.51 – -4.18	0.080
variance_minferet:median_shape_factor	-47.22	-106.68 – 12.24	0.158
Muscle:median_shape_factor	-113.72	-232.23 – 4.79	0.097
variance_minferet:Musclesol:median_shape_factor	196.48	0.50 – 392.46	0.085
Observations	16		
R^2 / R^2 adjusted	0.775 / 0.578		
F-statistic	3.93 on 7 and 8 DF		
p-value	0.03692		

Table 4.1: Multiple Regression predicting membrane strain

4.4 Discussion

The goal of this work was to create a new skeletal muscle image processing software that accurately and efficiently create finite-element models based on muscle cross sectional images, and to use that software to develop image-based micromechanical models of muscle to determine the effects of variations in muscle microstructure on the macroscopic behavior and muscle damage susceptibility. By utilizing a custom novel-image segmentation software and mapping each pixel within the image to a unique hexahedral element, writing custom matlab code to automatically generate the Febio finite element models, and running the models on an 8 core 240 GB computing cluster, this modeling framework has allowed for the simulation of an unprecedented number of large finite element models. While previous work has built micromechanical models of muscle ranging from 7-25 fibers, to our knowledge no

other work has built micromechanical models of whole muscle cross-sections containing hundreds of muscle fibers.

It is important to consider a number of limitations to the models presented here. First, both sectioning of muscles and image processing can introduce errors into the model. While we excluded from analysis any muscle cross-sections with sectioning artifacts or holes, we acknowledge that errors at either of these stages could propagate error throughout the modeling framework. Furthermore, the ECM was considered to be a continuous structure throughout the micromechanical model with the same constitutive model used for both the endomysium and perimysium components. However, previous research has indicated that these layers may have different collagen compositions, and therefore different material behaviors. Additionally, our constitutive model of ECM did not account for the varying collagen directions seen in ECM. Preliminary research from the Blemker lab has indicated that collagen may display orientations perpendicular to muscle fibers. If so, both more research quantifying the direction of collagen in ECM as well as material behaviors would be needed to more accurately replicate the behavior of ECM within the micromechanical models. Additionally, we represented the mechanical properties of the sarcolemma transmembrane proteins using a continuous nonlinear curve, whereas other physiological models of transmembrane proteins have used a piecewise function due to the unfolding of the protein [61], [62]. Sensitivity analysis of the coefficient term used in the nonlinear spring equation to represent dystrophin showed that a 10 percent change in coefficient term, changed the average membrane strain for each cross section by an average of 2.1 percent (Figure 4.7).

The micromechanical models presented in this chapter focused on the behavior of dystrophic and wild-type muscle in simple shear as the shearing of the muscle cross-section is the dominant mode of lateral force transmission in muscle, and the shear behavior can be inferred from muscle's microstructure. However, we acknowledge that our

models are limited by the fact that simple shear does not fully represent physiological loading patterns of muscle.

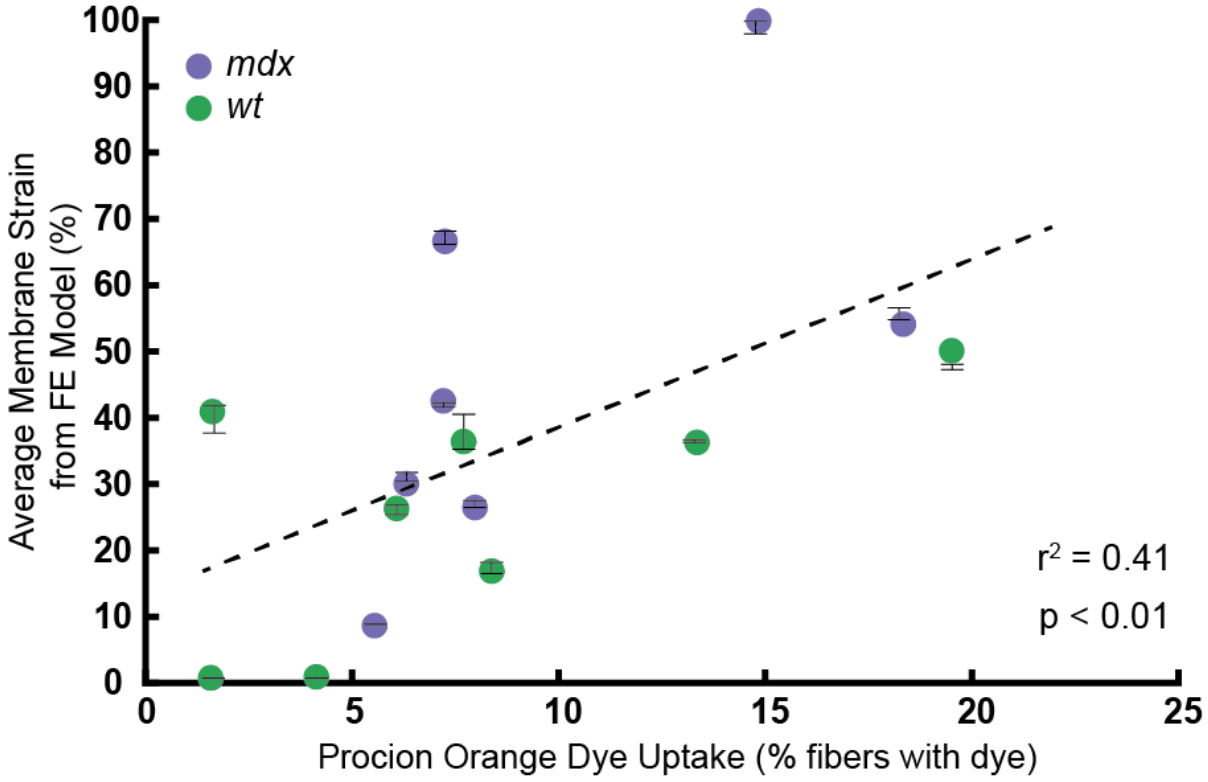

Figure 4. 8: Sensitivity Analysis of Dystrophin Spring Constant. The dystrophin spring constant was altered by both positive and negative percent and FE simulations were rerun. Error bars represent the change in membrane strain based upon the sensitivity analysis simulations.

Ultimately, our results suggest that micromechanical muscle models are predictive of membrane damage in both healthy and diseased muscles. Furthermore, our results suggest that muscle fiber circularity, area, minimum feret's diameter, and the variance of muscle fiber sizes and minimum feret's diameters within a muscle may contribute to a given muscle's susceptibility to damage. This model-experiment integration provides a framework to determine micro-scale damage from microstructure images and could be used to ultimately predict the effects of pharmacological treatments on the susceptibility of DMD muscles to damage.

Chapter 5

Thesis Discussion and Future Directions

This thesis was originally motivated by my desire to create an image processing tool that greatly speeds up the process of skeletal muscle image analysis. Following the creation of the algorithm, I realized that there was an opportunity to couple the image processing algorithm to micromechanical finite element modeling to investigate the role of microstructure variations on the damage susceptibility of both wild-type and dystrophic muscles. Duchenne muscular dystrophy is a complex disorder wherein multiple confounding factors contribute to disease progression. By coupling and automating a framework to move from skeletal muscle cross-sectional images to micromechanical finite element models, I have created more realistic and larger scale micromechanical finite element models than has been previously attempted. Computational models such as these have the power to answer questions such as: how does variation of muscle fiber sizes affect the damage susceptibility of muscle and does fiber circularity affect damage. Ultimately, this model-experiment integration provides a framework to determine micro-scale damage from microstructure images and could be used to ultimately predict the effects of pharmacological treatments on the susceptibility of DMD muscles to damage.

5.1 Contributions

I have created the first micromechanical models of full skeletal muscle cross-sections, based upon real muscle histological images. While previous work has created micromechanical models to derive tissue level constitutive properties from muscle

microstructures and understand how disease adaptations in Duchenne muscular dystrophy affect tissue level function, neither of these models were based upon full muscle cross-sections. My work coupling an automatic skeletal image analysis algorithm to an automated approach to generated finite element models provides an integrated experiment-modeling framework for relating real muscle microstructure to muscle function. While this work built from the micromechanical modeling work from Virgilio et al., Virgilio used an agent-based model to generate small muscle fascicles (consisting of few muscle fibers), as opposed to directly creating the models from real images [4]. I have created a more accessible framework for micromechanical modeling by coupling my Matlab image proceeding algorithm to a custom Matlab algorithm that generates and outputs Febio finite element micromechanical models. By automating the generation of FE micromechanical models from muscle-cross-sectional images, it is possible for other users to generate their own micromechanical models with very little effort, as analysis of membrane strain after FE simulation has also been automated.

Using micromechanical models, we can predict strains experienced by the fibers at the micro-scale level to provide insight into the likelihood of fiber damage and the initiation of injury. From our models' results, we found that membrane strain in micromechanical modeling correlates with an experimental index of muscle damage, thereby supporting the use of micromechanical modeling to establish a direct link between muscle microstructures and changes in macro-scale muscle function. Our results also showed that susceptibility to damage varies widely across muscles, even within the same mouse strain. Muscles that were more susceptibility to damage displayed increases in the variation of muscle fiber areas and minimum feret's diameters within a cross-section.

An additional contribution of this work is the novel skeletal-muscle analysis algorithm that significantly improves upon the efficiency of previously open-sourced algorithms. In particular, the most valuable aspect of the algorithm is its ability to batch

process images. Current muscle analyses software programs require a user to sit a computer and input an image for each analysis that is desired. Allowing for batch processing allows for a user to run analyses overnight or when doing other things, thereby saving researchers hours of analysis time that would otherwise be required.

5.1 Future Work

For the skeletal muscle analysis imaging algorithm, future improvements could involve the generation of a convolutional neural network. Combining the algorithm with a manual adjustment of segmentations could allow for a training set of "perfect" muscle segmentations to be created of muscle in various injured or healthy states. Using this training set, a convolutional neural net could be created and evaluated using a portion of that set to train the convolutional neural net, and another portion to test accuracy and robustness.

As this thesis provides a tool to automate the generation of micromechanical finite element models, it can serve as a platform for future studies to build off of and suggest new insights into muscle structure-function relationships at the microscopic level. The long-term goal of the work presented in this thesis is to better understand the role that muscle microstructure plays in the chronic degeneration that occurs in DMD. Furthermore, this work has laid the foundations to quantify the relationship between membrane strain and muscle damage. This work could be used to create a computational model that couples image analysis, agent-based modeling, and finite element modeling to simulate muscle degeneration over time in the *mdx* mouse. Agent-based models of muscle degeneration have previously been published that predict the dynamic regenerative response of muscle fibers, fibroblasts, SSCs, and inflammatory cells as a result of a single acute contraction-induced injury in dystrophic muscle. Future work could modify this algorithm to predict muscle

degeneration throughout the lifespan of the *mdx* mouse by utilizing the skeletal muscle image analysis algorithm for validation.

Future iterations to the micromechanical modeling approach presented here could involve recapitulating the behavior of ECM in a more realistic way. To do so, experiments quantifying both the direction of collagen in ECM as well as ECM stiffness are needed. Ongoing work within our lab by Ridhi Sahani hopes to quantify collagen direction in ECM utilizing scanning electron microscopy. Additional experiments could quantify collagen stiffness utilizing biaxial mechanical testing experiments to determine the shear passive properties of the tissue. The ultimate goal of the work presented here would be to generate computational models that could *in silico* test therapeutics for DMD. As DMD is a complex, multifaceted disease *in silico* testing will most likely involve a coupling of a model predicting cell regenerative and inflammatory behavior to a finite element model of muscle degeneration. The micromechanical models and image-analysis software presented in this thesis are the ground work need for future work in *in silico* testing of therapeutics for Duchenne muscular dystrophy. I believe that computational models provide a powerful paradigm to understand muscle degeneration and explore possible treatment approaches for Duchenne muscular dystrophy (DMD) and hope that this work lays a foundation for the creation of future treatments for boys living with DMD today.

Bibliography

[1] E. P. Hoffman, R. H. Brown, and L. M. Kunkel, “Dystrophin: The protein product of the duchenne muscular dystrophy locus,” *Cell*, vol. 51, no. 6, pp. 919–928, Dec. 1987.

[2] K. P. García-Pelagio, R. J. Bloch, A. Ortega, and H. González-Serratos, “Biomechanics of the sarcolemma and costameres in single skeletal muscle fibers from normal and dystrophin-null mice.,” *J. Muscle Res. Cell Motil.*, vol. 31, no. 5–6, pp. 323–36, Mar. 2011.

[3] B. J. Petrof, “The molecular basis of activity-induced muscle injury in Duchenne muscular dystrophy,” *Mol. Cell. Biochem.*, vol. 179, no. 1/2, pp. 111–124, 1998.

[4] K. M. Virgilio, K. S. Martin, S. M. Peirce, and S. S. Blemker, “Multiscale models of skeletal muscle reveal the complex effects of muscular dystrophy on tissue mechanics and damage susceptibility,” *Interface Focus*, vol. 5, no. 2, p. 20140080, Apr. 2015.

[5] M. McLeod, L. Breen, D. L. Hamilton, and A. Philp, “Live strong and prosper: the importance of skeletal muscle strength for healthy ageing.,” *Biogerontology*, vol. 17, no. 3, pp. 497–510, 2016.

[6] K. M. Kim, H. C. Jang, and S. Lim, “Differences among skeletal muscle mass indices derived from height-, weight-, and body mass index-adjusted models in assessing sarcopenia,” *Korean J. Intern. Med.*, vol. 31, no. 4, p. 643, Jul. 2016.

[7] C. C. Henry, K. S. Martin, B. B. Ward, G. G. Handsfield, S. M. Peirce, and S. S. Blemker, “Spatial and age-related changes in the microstructure of dystrophic and healthy diaphragms.,” *PLoS One*, vol. 12, no. 9, p. e0183853, 2017.

[8] A. Ishihara, F. Nagatomo, M. Terada, H. Fujino, H. Kondo, and N. Ishioka, “Effects of microgravity on the mouse triceps brachii muscle,” *Muscle Nerve*, vol. 52, no. 1, pp. 63–68, Jul. 2015.

[9] K. Bushby *et al.*, “Diagnosis and management of Duchenne muscular dystrophy, part 1: diagnosis, and pharmacological and psychosocial management,” *Lancet Neurol.*, vol. 9, no. 1, pp. 77–93, Jan. 2010.

[10] Q. Q. Gao and E. M. McNally, “The Dystrophin Complex: Structure, Function, and Implications for Therapy.,” *Compr. Physiol.*, vol. 5, no. 3, pp. 1223–39, Jul. 2015.

[11] C. M. Consolino and S. V. Brooks, “Susceptibility to sarcomere injury induced by single stretches of maximally activated muscles of *mdx* mice,” *J. Appl. Physiol.*, vol. 96, no. 2, pp. 633–638, Feb. 2004.

[12] S. M. Mijailovich, O. Kayser-Herold, B. Stojanovic, D. Nedic, T. C. Irving, and M. A. Geeves, "Three-dimensional stochastic model of actin–myosin binding in the sarcomere lattice," *J. Gen. Physiol.*, vol. 148, no. 6, pp. 459–488, Dec. 2016.

[13] I. Pertici, M. Caremani, and M. Reconditi, "A mechanical model of the half-sarcomere which includes the contribution of titin," *J. Muscle Res. Cell Motil.*, pp. 1–13, Mar. 2019.

[14] F. Sahli Costabal, J. Yao, and E. Kuhl, "Predicting drug-induced arrhythmias by multiscale modeling," *Int. j. numer. method. biomed. eng.*, vol. 34, no. 5, p. e2964, May 2018.

[15] S. S. Blemker and S. L. Delp, "Three-dimensional representation of complex muscle architectures and geometries.," *Ann. Biomed. Eng.*, vol. 33, no. 5, pp. 661–73, May 2005.

[16] D. G. Thelen, "Adjustment of muscle mechanics model parameters to simulate dynamic contractions in older adults.," *J. Biomech. Eng.*, vol. 125, no. 1, pp. 70–7, Feb. 2003.

[17] B. Sharafi and S. S. Blemker, "A micromechanical model of skeletal muscle to explore the effects of fiber and fascicle geometry," *J. Biomech.*, vol. 43, no. 16, pp. 3207–3213, Dec. 2010.

[18] B. Sharafi and S. S. Blemker, "A mathematical model of force transmission from intrafascicularly terminating muscle fibers," *J. Biomech.*, vol. 44, no. 11, pp. 2031–2039, Jul. 2011.

[19] B. Sharafi, E. G. Ames, J. W. Holmes, and S. S. Blemker, "Strains at the myotendinous junction predicted by a micromechanical model," *J. Biomech.*, vol. 44, no. 16, pp. 2795–2801, Nov. 2011.

[20] E. K. Moo, T. R. Leonard, and W. Herzog, "In Vivo Sarcomere Lengths Become More Non-uniform upon Activation in Intact Whole Muscle," *Front. Physiol.*, vol. 8, p. 1015, Dec. 2017.

[21] J. M. Squire, "Architecture and function in the muscle sarcomere," *Curr. Opin. Struct. Biol.*, vol. 7, no. 2, pp. 247–257, Apr. 1997.

[22] H. E. Huxley, "The mechanism of muscular contraction.," *Science*, vol. 164, no. 3886, pp. 1356–65, Jun. 1969.

[23] F. E. Zajac, "Muscle and tendon: properties, models, scaling, and application to biomechanics and motor control.," *Crit. Rev. Biomed. Eng.*, vol. 17, no. 4, pp. 359–411, 1989.

[24] R. L. Lieber, E. Runesson, F. Einarsson, and J. Fridén, "Inferior mechanical properties of spastic muscle bundles due to hypertrophic but compromised extracellular matrix material," *Muscle Nerve*, vol. 28, no. 4, pp. 464–471, Oct. 2003.

[25] P. P. Purslow, “The structure and functional significance of variations in the connective tissue within muscle.,” *Comp. Biochem. Physiol. A. Mol. Integr. Physiol.*, vol. 133, no. 4, pp. 947–66, Dec. 2002.

[26] R. L. Lieber, S. Steinman, I. A. Barash, and H. Chambers, “Structural and functional changes in spastic skeletal muscle,” *Muscle Nerve*, vol. 29, no. 5, pp. 615–627, May 2004.

[27] C. Pasternak, S. Wong, and E. L. Elson, “Mechanical function of dystrophin in muscle cells.,” *J. Cell Biol.*, vol. 128, no. 3, pp. 355–61, Feb. 1995.

[28] J. M. Ervasti, “Costameres: the Achilles’ heel of Herculean muscle.,” *J. Biol. Chem.*, vol. 278, no. 16, pp. 13591–4, Apr. 2003.

[29] D. J. Blake, A. Weir, S. E. Newey, and K. E. Davies, “Function and Genetics of Dystrophin and Dystrophin-Related Proteins in Muscle,” *Physiol. Rev.*, vol. 82, no. 2, pp. 291–329, Apr. 2002.

[30] S. L. Delp, K. Statler, and N. C. Carroll, “Preserving plantar flexion strength after surgical treatment for contracture of the triceps surae: A computer simulation study,” *J. Orthop. Res.*, vol. 13, no. 1, pp. 96–104, Jan. 1995.

[31] G. G. Handsfield, K. R. Knaus, N. M. Fiorentino, C. H. Meyer, J. M. Hart, and S. S. Blemker, “Adding muscle where you need it: non-uniform hypertrophy patterns in elite sprinters,” *Scand. J. Med. Sci. Sports*, vol. 27, no. 10, pp. 1050–1060, Oct. 2017.

[32] S. S. Blemker and S. L. Delp, “Rectus femoris and vastus intermedius fiber excursions predicted by three-dimensional muscle models,” *J. Biomech.*, vol. 39, no. 8, pp. 1383–1391, Jan. 2006.

[33] N. M. Fiorentino and S. S. Blemker, “Musculotendon variability influences tissue strains experienced by the biceps femoris long head muscle during high-speed running.,” *J. Biomech.*, vol. 47, no. 13, pp. 3325–33, Oct. 2014.

[34] A. F. HUXLEY and R. NIEDERGERKE, “Structural Changes in Muscle During Contraction: Interference Microscopy of Living Muscle Fibres,” *Nature*, vol. 173, no. 4412, pp. 971–973, May 1954.

[35] A. V. Hill, “The heat of shortening and the dynamic constants of muscle,” *Proc. R. Soc. London. Ser. B - Biol. Sci.*, vol. 126, no. 843, pp. 136–195, Oct. 1938.

[36] S. L. Delp and J. P. Loan, “A computational framework for simulating and analyzing human and animal movement,” *Comput. Sci. Eng.*, vol. 2, no. 5, pp. 46–55, 2000.

[37] A. Seth *et al.*, “OpenSim: Simulating musculoskeletal dynamics and neuromuscular control to study human and animal movement,” *PLOS Comput. Biol.*, vol. 14, no. 7, p. e1006223, Jul. 2018.

[38] R. R. Lemos, M. Epstein, W. Herzog, and B. Wyvill, "A Framework for Structured Modeling of Skeletal Muscle," *Comput. Methods Biomech. Biomed. Engin.*, vol. 7, no. 6, pp. 305–317, Dec. 2004.

[39] G. E. Norte *et al.*, "MRI-Based Assessment of Lower-Extremity Muscle Volumes in Patients Before and After ACL Reconstruction," *J. Sport Rehabil.*, vol. 27, no. 3, pp. 201–212, May 2018.

[40] S. S. Blemker, P. M. Pinsky, and S. L. Delp, "A 3D model of muscle reveals the causes of nonuniform strains in the biceps brachii," *J. Biomech.*, vol. 38, no. 4, pp. 657–665, Apr. 2005.

[41] S. Nemat-Nasser and M. (Muneo) Hori, *Micromechanics : overall properties of heterogeneous materials*. .

[42] P. A. Huijing, "Muscle as a collagen fiber reinforced composite: a review of force transmission in muscle and whole limb.," *J. Biomech.*, vol. 32, no. 4, pp. 329–45, Apr. 1999.

[43] L. A. Spyrou, S. Brisard, and K. Danas, "Multiscale modeling of skeletal muscle tissues based on analytical and numerical homogenization," *J. Mech. Behav. Biomed. Mater.*, vol. 92, pp. 97–117, Apr. 2019.

[44] J. A. Weiss, B. N. Maker, and S. Govindjee, "Finite element implementation of incompressible, transversely isotropic hyperelasticity," *Comput. Methods Appl. Mech. Eng.*, vol. 135, no. 1–2, pp. 107–128, Aug. 1996.

[45] J. C. Criscione, A. S. Douglas, and W. C. Hunter, "Physically based strain invariant set for materials exhibiting transversely isotropic behavior," *J. Mech. Phys. Solids*, vol. 49, no. 4, pp. 871–897, Apr. 2001.

[46] T. M. Best, J. McElhaney, W. E. Garrett, and B. S. Myers, "Characterization of the passive responses of live skeletal muscle using the quasi-linear theory of viscoelasticity.," *J. Biomech.*, vol. 27, no. 4, pp. 413–9, Apr. 1994.

[47] L. R. Smith and E. R. Barton, "SMASH – semi-automatic muscle analysis using segmentation of histology: a MATLAB application," *Skelet. Muscle*, vol. 4, no. 1, p. 21, Nov. 2014.

[48] Y. Wen *et al.*, "MyoVision: software for automated high-content analysis of skeletal muscle immunohistochemistry.," *J. Appl. Physiol.*, vol. 124, no. 1, pp. 40–51, Jan. 2018.

[49] P. Suetens, R. Verbeeck, D. Delaere, J. Nuyts, and B. Bijnens, "Model-Based Image Segmentation: Methods and Applications," Springer, Berlin, Heidelberg, 1991, pp. 3–24.

[50] Liu Jianzhuang, Li Wenqing, and Tian Yupeng, “Automatic thresholding of gray-level pictures using two-dimension Otsu method,” in *1991 International Conference on Circuits and Systems*, 1991, pp. 325–327.

[51] P. F. Felzenszwalb and D. P. Huttenlocher, “Efficient Graph-Based Image Segmentation,” *Int. J. Comput. Vis.*, vol. 59, no. 2, pp. 167–181, Sep. 2004.

[52] A. Bleau and L. J. Leon, “Watershed-Based Segmentation and Region Merging,” *Comput. Vis. Image Underst.*, vol. 77, no. 3, pp. 317–370, Mar. 2000.

[53] D. L. Collins, C. J. Holmes, T. M. Peters, and A. C. Evans, “Automatic 3-D model-based neuroanatomical segmentation,” *Hum. Brain Mapp.*, vol. 3, no. 3, pp. 190–208, Jan. 1995.

[54] K. Zuiderveld, “Graphics Gems IV,” P. S. Heckbert, Ed. San Diego, CA, USA: Academic Press Professional, Inc., 1994, pp. 474–485.

[55] A. A. Taha and A. Hanbury, “Metrics for evaluating 3D medical image segmentation: analysis, selection, and tool.,” *BMC Med. Imaging*, vol. 15, p. 29, Aug. 2015.

[56] K. H. Zou *et al.*, “Statistical validation of image segmentation quality based on a spatial overlap index.,” *Acad. Radiol.*, vol. 11, no. 2, pp. 178–89, Feb. 2004.

[57] X. Hu, J. P. Charles, T. Akay, J. R. Hutchinson, and S. S. Blemker, “Are mice good models for human neuromuscular disease? Comparing muscle excursions in walking between mice and humans,” *Skelet. Muscle*, vol. 7, no. 1, p. 26, Dec. 2017.

[58] S. V. BROOKS, “Rapid recovery following contraction-induced injury to in situ skeletal muscles in mdx mice,” *J. Muscle Res. Cell Motil.*, vol. 19, no. 2, pp. 179–187, 1998.

[59] G. S. Lynch, J. A. Rafael, J. S. Chamberlain, and J. A. Faulkner, “Contraction-induced injury to single permeabilized muscle fibers from *mdx* , transgenic *mdx* , and control mice,” *Am. J. Physiol. Physiol.*, vol. 279, no. 4, pp. C1290–C1294, Oct. 2000.

[60] C. Dellorusso, R. W. Crawford, J. S. Chamberlain, and S. V. Brooks, “Tibialis anterior muscles in mdx mice are highly susceptible to contraction-induced injury,” *J. Muscle Res. Cell Motil.*, vol. 22, no. 5, pp. 467–475, 2001.

[61] N. Bhasin *et al.*, “Molecular Extensibility of Mini-dystrophins and a Dystrophin Rod Construct,” *J. Mol. Biol.*, vol. 352, no. 4, pp. 795–806, Sep. 2005.

[62] C. Zhang and Y. Gao, “The role of transmembrane proteins on force transmission in skeletal muscle,” *J. Biomech.*, vol. 47, no. 12, pp. 3232–3236, Sep. 2014.

[63] K. Matsumura and K. P. Campbell, “Dystrophin-glycoprotein complex: Its role in the molecular pathogenesis of muscular dystrophies,” *Muscle Nerve*, vol. 17, no. 1, pp. 2–15, Jan. 1994.

[64] A. Briguet, I. Courdier-Fruh, M. Foster, T. Meier, and J. P. Magyar, “Histological parameters for the quantitative assessment of muscular dystrophy in the mdx-mouse,” *Neuromuscul. Disord.*, vol. 14, no. 10, pp. 675–682, Oct. 2004.

[65] R. Nilwik *et al.*, “The decline in skeletal muscle mass with aging is mainly attributed to a reduction in type II muscle fiber size,” *Exp. Gerontol.*, vol. 48, no. 5, pp. 492–498, May 2013.

[66] P. Moens, P. H. W. W. Baatsen, and G. Marchal, “Increased susceptibility of EDL muscles from mdx mice to damage induced by contractions with stretch,” *J. Muscle Res. Cell Motil.*, vol. 14, no. 4, pp. 446–451, Aug. 1993.

[67] G. L. Warren, D. A. Hayes, D. A. Lowe, J. H. Williams, and R. B. Armstrong, “Eccentric contraction-induced injury in normal and hindlimb-suspended mouse soleus and EDL muscles.,” *J. Appl. Physiol.*, vol. 77, no. 3, pp. 1421–30, Sep. 1994.